Chapter 3

WIND GYRES

A central problem in the theory of oceanic circulation is wind-driven gyres between east and west bounding continents. As described in Chap. 1, this problem is relevant to the observed basin-scale gyres in the North and South Pacific, North and South Atlantic, and South Indian Oceans. The solution to the wind-gyre problem includes the Sverdrup Transport (for the vertically integrated horizontal flow away from the western boundary and any other sites of strong, narrow currents), as part of the answer. However, this is not a valid solution for the whole domain (*n.b.,* it does not satisfy the western boundary condition of no-normal flow); it also does not encompass any time variability; and it is only a linear, diagnostic relation rather than a nonlinear, prognostic one.

As a theoretical problem — as opposed to realistic simulation with an OGCM — the wind-gyre problem is typically idealized in several ways:

- simple basin shape (often a rectangular box)

- simple steady wind field

- no surface buoyancy forcing (*i.e.,* adiabatic).

Even with these simplifications the problem is a difficult one: the steady circulations are unstable (*i.e.,* this is yet another problem of turbulent equilibrium dynamics), and there are now known to be a variety of appreciably different regimes depending on the particulars of posing the problem. Many of the interesting versions of the wind-gyre problem defy an analytic solution, and computational solutions are needed. Nevertheless, this problem remains the focus of much attention because of its central importance in circulation theory.

1   Linear Barotropic Dynamics

The simplest completion of the Ekman-Sverdrup theory for wind gyres is the addition of frictional effects to the depth-integrated planetary vorticity equation. The simplest representation of friction is as a linear differential operator acting on the barotropic streamfunction. This can then be accommodated in a linear, barotropic potential vorticity equation with forcing and damping:

$$\frac{Dq}{Dt} \approx \frac{\partial \zeta}{\partial t} + \beta v = \frac{1}{H} curl\, \boldsymbol{\tau} - r\zeta + \nu \nabla^2 \zeta\,, \tag{1}$$

where H is the fluid depth, τ is the surface wind stress, ν is the lateral eddy viscosity (as a parameterization of horizontal Reynolds stress), r is the decay rate associated with bottom drag (*e.g.,* $r = \sqrt{\nu_v f_o/2}/H$ for a flat-bottom Ekman layer), $\zeta = \nabla^2\psi$ is the vertical vorticity, ψ is the barotropic (depth-averaged) streamfunction (with $u = -\psi_y$ and $v = \psi_x$), and

$$q = f(y) + \zeta \tag{2}$$

is the barotropic potential vorticity, with $f = f_0 + \beta y$ as a *beta*-plane approximation.

Steady solutions can be found for (1) in an enclosed basin when either ν or r is nonzero. The lateral boundary conditions are $\psi = 0$ and, if $nu \neq 0$, either free-slip, $\zeta = 0$, or no-slip, $\partial_{x_\perp}\psi = 0$ (where $x_\perp$ is a horizontal coordinate normal to the boundary).[1] The problem with only $r \neq 0$ was first solved in Stommel (1948) and the one with only $\nu \neq 0$ in Munk (1950), and these solutions are essentially similar. Because all nonlinear, turbulent, wind-gyre solutions require $\nu \neq 0$ (or its functional equivalent in dissipating the enstrophy cascade), we focus here on the Munk problem. In this case we rewrite (1) as

$$\nu\nabla^4\psi - \beta\psi_x = -\frac{1}{H}curl\,\boldsymbol{\tau}\,, \tag{3}$$

with no-slip boundary conditions,

$$\psi = \frac{\partial\psi}{\partial x_\perp} = 0\,. \tag{4}$$

The solution is obtained by a boundary-layer asymptotic approximation method. In the interior we assume the influence of eddy diffusion is negligible. This implies that the solution is approximately the Sverdrup solution (Sverdrup, 1947):

$$\psi^{sv}(x,y) = -\frac{1}{\beta H}\int_x^{x_e(y)} dx'\,curl\,\boldsymbol{\tau}(x',y)\,, \tag{5}$$

where $x = x_e(y)$ is the location of the eastern boundary. We set $\psi^{sv}(x_e,y) = 0$ at the eastern boundary, with the benefit of hindsight: the analysis just below shows that a complete eastern boundary layer cannot exist for (3) since there is only one homogeneous solution that decays to zero towards the interior whereas (4) requires two such solutions.

Thus, the complete solution requires the addition of boundary-layer components to the Sverdrup interior solution to satisfy the boundary conditions:

$$\psi = \psi^{sv}(x,y) + \psi^{bl}(\xi,\eta)\,. \tag{6}$$

Here local normal and tangential boundary-layer coordinates are defined by

$$\xi = \delta^{-1}(x_\perp - x_{\perp o})\,, \quad \eta = x_\|\,, \tag{7}$$

---

[1]It is a physically subtle question what the most appropriate lateral boundary conditions ought to be in a barotropic model of the ocean, since the real ocean has only a sloping bottom that rises to the coastline, not the vertical side wall that is assumed in every large-scale ocean model, even baroclinic ones, for at least some vertical interval of 10s to 1000s of meters. This important parameterization problem for numerical oceanic models is still largely unsolved.

and the boundary location is $x_\perp = x_{\perp o}(x_\parallel)$. The width of the boundary layer is δ, and in this asymptotic method δ is assumed to be much smaller than the width of the domain L. Substituting (6) into (3)-(4) yields the following local boundary-value problem in its boundary-layer approximation:

$$
\begin{aligned}
\psi^{bl}_{4\xi} - \frac{\beta\delta^3}{\nu}\psi^{bl}_\xi &= \mathcal{O}(\frac{\delta}{L}) \approx 0 \\
\psi^{bl}(0,\eta) &= -\psi^{sv}(bdy) \\
\psi^{bl}_\xi(0,\eta) &= -\delta\psi^{sv}_{x_\perp}(bdy) \approx 0 \\
\psi^{bl}(|\xi| \to \infty) &\to 0 .
\end{aligned}
\tag{8}
$$

For the ODE to have a well-ordered, non-trivial solution, we choose

$$
\delta = \left(\frac{\nu}{\beta}\right)^{1/3} .
\tag{9}
$$

The solutions of (8) are of the form

$$
\psi^{bl} \propto e^{\lambda\xi}, \quad \lambda^3 = 1 ,
\tag{10}
$$

with the real part of λ negative satisfying the decay condition as $|\xi| \to \infty$. For $\xi \to +\infty$, there are two homogeneous solutions, with

$$
\lambda_\pm = e^{\pm i 2\pi/3} ,
\tag{11}
$$

and

$$
\psi^{bl} = -\frac{1}{2}\psi^{sv}(bdy)\left(e^{\lambda_+\xi} + e^{\lambda_-\xi}\right) .
\tag{12}
$$

For $\xi \to -\infty$, there is only one λ root with a positive real part. However, since $\psi^{bl} = \mathcal{O}(\delta/L) \approx 0$ on the eastern boundary, this suffices because there the interior solution already satisfies the condition of no normal flow there. In general, both for (1) and its baroclinic generalizations, there is less freedom to satisfy boundary-layer conditions on the eastern boundaries, because $\beta > 0$ on Earth. This gives a basis for understanding why real wind gyres have stronger western boundary currents (WBC) than eastern ones.

An application of this solution to the North Pacific Ocean is shown in Fig. 2, based upon an empirical estimate for the time- and zonal-mean zonal wind stress. We see the NECC and the sub-tropical and sub-polar gyres. The value of ν is chosen such that δ has about the right width for the WBC. For $\delta = 50$ km and $\beta = 2 \times 10^{-11}$ m^{-1} s^{-1}, then $\nu = 2.5 \times 10^3$ m^2 s^{-1}. This value is too small to allow the resolution of such a narrow WBC in a coarse-resolution OGCM with a horizontal grid size of $\mathcal{O}(100)$ km. (It is also much smaller than is required for computational stability of such a model.) Consequently these models use larger values of ν (Chap. 7), and their solutions, which do have Munk-like boundary current dynamics, have WBCs that are several hundred km wide.

2 Nonlinear Barotropic Dynamics

We can more generally solve the barotropic potential vorticity equation (1) without linearizing the potential-vorticity advection,

$$\frac{Dq}{Dt} = \zeta_t + J[\psi, \zeta] + \beta v = \frac{1}{H} curl\,\boldsymbol{\tau} + \nu \nabla^2 \zeta - r\zeta \,, \tag{13}$$

where the vorticity advection operator is the horizontal Jacobian, $J[A, B] = A_x B_y - A_y B_x$. The lateral boundary conditions are the same as in the preceeding linear problem (*e.g.,* no-normal flow and (4) for no-slip).

We again seek steady solutions for steady wind stress. Based on the previous linear solutions, we might anticipate that the interior solution will still be ψ^{sv} in (5). This presumes that we can still find consistent boundary-layer corrections to it, as in the linear Munk problem when the nonlinear effects are significant at least in the boundary layers. There are three different types of western boundary-layer balances that can arise in (13), each with its characteristic boundary-layer width that can be estimated by scale analysis:

<u>Munk (1950)</u> $\qquad \beta v \approx \nu \zeta_{xx}$ $\qquad\qquad\qquad\qquad\qquad\qquad\qquad\qquad \Rightarrow \delta_m = \left(\frac{\nu}{\beta}\right)^{1/3}$

<u>Stommel (1948)</u> $\quad \beta v \approx -r\zeta$ $\qquad\qquad\qquad\qquad\qquad\qquad\qquad\qquad \Rightarrow \delta_s = \left(\frac{r}{\beta}\right)$

<u>Charney (1955)</u> $\quad J(\psi, q) \approx 0 \qquad \Rightarrow q(x,y) \approx Q[\psi(x,y)]$

$\qquad \psi_{xx} + \beta y \approx Q[\psi] \equiv -\frac{\beta}{U_o}\psi$ if $\psi \to -U_o y,\ U_o < 0$, as $x \to \infty$ $\qquad \Rightarrow \delta_c = \left(-\frac{U_o}{\beta}\right)^{1/2}$.

The sign constraint on the zonal inflow to the western boundary current in the latter case arises again,from the requirement that there exist boundary-layer solutions that decay toward the east into the gyre interior. Of course, these balances also can occur in various combinations if the δ values coincide. (All of these papers appear in the book by Robinson (1963).)

The nonlinear type of balance above is called an *inertial boundary layer*. More general functional relationships $Q[\psi]$ are also possible, but the linear relationship here is the easiest to analyze. This balance only occurs at latitudes where the interior flow is westward into the boundary layer, while whereas the Sverdrup solution (5) will match this condition only at some latitudes. This gives us a hint that nonlinear effects will be important more extensively than just within the WBC. One possible reconciliation of these conflicting requirements is that the interior solution differ from (5) to provide westward boundary-layer inflow at almost all latitudes, except where the WBC separates from the coast as a narrow eastward jet; as we will see below, this at least partially occurs when the WBC is significantly inertial (*i.e.,* when $\delta_c \gg, \delta_m,\ \delta_s$).

Before examining solutions of (13), we note that there exists a class of steady, conservative solutions, whose first example was found by Fofonoff (1954). In it the linear functional relation

$Q[\psi]$ holds everywhere in the domain, not just in the boundary layer:

$$\nabla^2 \psi + \beta y \;=\; Q[\psi] \;\equiv\; -\frac{\beta}{U_o}\psi\,, \tag{14}$$

so that the advective term in (13) vanishes to leading order. This might be an appropriate approximation for strong flows with weak forcing and dissipation, if these latter effects could be appended to the solution of (14) in a regular perturbative way. The solution of (14) is plotted in Fig. 3 for the configuration of a single gyre with the strongest eastward currents at its northern edge (somewhat as in a sub-tropical gyre in the northern hemisphere). Note that the interior flow is everywhere westward,

$$\psi \to -U_o y,\ U_o < 0\,, \tag{15}$$

and there are inertial boundary layers of width δ_c on the both the east and west sides of the domain, as well as on at least one of the north or south side. A boundary-layer approximation to the solution of (14) along any zonal interior line is

$$\psi(x,y) \;\approx\; U_o \left(L_y \exp\left[-\frac{y - L_y}{\delta_c}\right] \;-\; y \right) \tag{16}$$

for $y\varepsilon[0, L_y]$. (Note that only the first boundary condition in (4) is satisfied by (16), consistent with the $\nu = 0$ approximation.) The shape of this gyre is quite different from the Munk solution (Fig. 2), as well as from the qualitatively similar shape of the Stommel solution. The problem of synthesizing the Munk/Stommel, Charney, and Fofonoff solutions — if it is even possible — is a classical one in oceanic circulation theory (as Fermat's last theorem used to be in mathematics). I was offered the chance to solve it for my Ph.D. thesis, and in retrospect I am quite glad I declined the offer in an era before computer solutions of (13) became routinely possible; the reason for this is the intrinsic transient variability — *i.e.,* the instability of steady solutions — that develops in the inertial regime.

Even if a solution to (13) has a strongly inertial character in its pointwise dynamical balances, *e.g.,* in the WBC, the forcing and dissipation terms are very important in the integral balances. To see this is we examine the integral balances for circulation and energy. We assume that the solution is in temporal equilibrium, either as a stable, steady circulation or as an unstable, time-averaged circulation with steady wind forcing and rectification effects by (mesoscale) eddies. We calculate a mean *circulation integral* by integrating the time-average of (13) over the area inside any closed contour of $\overline{\psi}(x,y)$; the result is that the time derivative and mean advection terms contribute nothing, and the remaining terms satisfy

$$\frac{1}{H} \oint \tau^{(s)}\, ds \;=\; -\nu \oint \overline{\zeta}_n\, ds + r \oint \overline{\psi}_n\, ds - \oint \overline{\psi'_s q'}\, ds\,. \tag{17}$$

Here (n, s) are local normal and tangential coordinates at the areal boundary, and the prime denotes a fluctuation about the time average. Thus, on each mean streamline, the integrated wind torque is balanced by mean drag and diffusion, plus the rectified eddy potential-vorticity flux, if any. Alternatively, we calculate the mean *energy balance* by multiplying (13) by $-\psi$, integrating

over the whole domain, and time-averaging. The result has no contributions from either the time derivative or advection (that merely rearranges energy density within the domain), and it expresses the balance between wind-work (the energy source) and dissipation (the energy sink),

$$-\frac{1}{H}\langle\overline{\psi}\,curl\,\boldsymbol{\tau}\rangle \;=\; \nu\langle\overline{\zeta^2}\rangle + r\langle\overline{(\boldsymbol{\nabla}\psi)^2}\rangle\,.\tag{18}$$

Angle brackets denote the area average.

For solutions with δ_c not small compared to the nonzero values of δ_m and δ_s, there is no known analytic solution for (13). However, this problem can be solved numerically, and several examples are shown in Figs. 4-9.

Figures 4-5 show steady, sub-tropical gyre solutions for progressively more inertial boundary currents. Note the northeastward shifts of the gyre center, an increasingly strong *recirculation zone* in the northwest part of the gyre with enhanced anti-cyclonic circulation above that in the Sverdrup interior circulation, and an increasing degree of curvature that develops in the streamlines. Notice that the effects of nonlinearity differ depending on whether ν or r provides the dominant dissipative mechanism. For solutions with $\nu = 0$ and $r \neq 0$, the gyre re-configuration with increasing δ_c/δ_s moves the pattern of zonal flow near the western boundary from the two-direction Sverdrup circulation to the westward-only circulation required for an inertial western boundary layer, and it also moves the pattern closer to the wholly conservative Fofonoff solution (Fig. 3). For solutions with $\nu \neq 0$ and $r = 0$, the pattern changes with increasing δ_c/δ_m, and it shows an complex streamline pattern in the northwest corner of the gyre. Solutions that are even more nonlinear, with larger δ_c or smaller δ_m and δ_s, lose stability due to their large lateral shear (*i.e.,* barotropic instability). They become intrinsically time-varying, and they approach a statistical-equilibrium energy balance among mean wind forcing, mean dissipation, and eddy rectification (*i.e.,* primarily a mean energy loss to eddy energy that in turn is balanced by dissipation of eddy energy).

As an alternative to the "real-fluid" choice of no-slip, (13) has also been posed with a free-slip boundary conditions. Free-slip solutions are shown in Figs. 6-9. For moderately nonlinear, single-gyre solutions (Fig. 6), this alternative boundary condition yields steady solutions with yet another characteristic gyre pattern, and it too includes an intensified recirculation zone in the northeast corner. With greater nonlinearity, however, a single-gyre solution can have multiple steady states for the same values of the wind-forcing and dissipation parameters (Fig. 7), and the stronger of the two solutions exhibits *inertial runaway* as the strength of the nonlinearity goes to infinity and all of the influences of β, τ, and $(r,\,\nu)$ become unimportant. This latter behavior is a steady, stable solution of (13) whose dominant balance is

$$J[\psi,\zeta] \;\approx\; 0 \quad\Rightarrow\quad \zeta \approx Z[\psi]\,.\tag{19}$$

If the latter relation is a linear functional (again, for mathematical tractability), then the solution form is

$$\psi(x,y) \;=\; \psi_o \sin\left[\pi x/L_x\right]\sin\left[\pi y/L_y\right],\tag{20}$$

which closely resembles the gyre pattern in Fig. 8. This gyre shape can exist only with $\nu = 0$ or the free-slip boundary condition.

Nevertheless, our general expectation is that wind-driven gyre solutions to (13) will usually become unstable as the boundary current dynamical balances become more inertial (due to either increasing wind stress or decreasing dissipation coefficients), so that rectification becomes significant in the mean dynamical balances. Of course, we are encouraged in this expectation by the ubiquitous observational evidence for energetic mesoscale eddies, particularly in the western parts of wind gyres; although mean gyre instability is not the only generation mechanism for eddies, it is generally accepted as the most important one.

In the circulation integral (17), the eddy flux (*viz.*, the integrated curl of the divergence of the horizontal Reynolds stress) can act to redistribute the wind-torque within a gyre. However, since the normal eddy flux vanishes at the solid boundary (where $\psi'_s = 0$), its cannot play this role for the integration circuit that coincides with the outermost streamline along the boundary. In the single-gyre problem, $curl\,\boldsymbol{\tau}$ is assumed to be everywhere of the same sign (*e.g.,* < 0 for a northern hemisphere sub-tropical gyre), so the mean flow must become very strong near the boundary as r and ν decrease in order to balance the wind torque; this is what happens in inertial runaway. However, for a multiple-gyre problem with open-ocean boundaries between gyres with $curl\,\boldsymbol{\tau}$ of different signs — in particular, the canonical *double-gyre* problem for adjacent sub-polar and sub-tropical gyres — the eddy fluxes resulting from instability can exchange cyclonic and anti-cyclonic potential vorticity between neighboring gyres, so that (17) can be satisfied for small r and ν even on the boundary integration circuit, without the mean circulation becoming excessively strong (*e.g.,* Fig. 9).

The energy balance (18) is satisfied with small r and ν in both single and multiple gyres either by a stable mean flow becoming sufficiently strong to provide large enough mean dissipation by itself, or by the eddy variances increasing the total dissipation sufficiently while the unstable mean circulation remains moderate in its strength (*e.g.,* as in Fig. 9).

3   Nonlinear Baroclinic Dynamics

We now consider how baroclinic effects alter the circulation of wind-driven gyres. The source of baroclinicity, of course, is the stable density stratification that ultimately is a product of the surface buoyancy forcing and thermohaline circulation (Chaps. 2 & 6). We will focus on intrinsically transient gyre dynamics that arise from mesoscale instability of the directly forced circulation. As we show below, gyre baroclinicity and transience are very closely associated with each other. Although intrinsic variability also arises in barotropic gyres for sufficiently weak diffusion or damping, its dynamical behavior is rather different than a 3D stratified ocean, hence less interesting as a model for nature. The topics covered here are also addressed in Young (1987) and Pedlosky (1996), albeit from somewhat different points of view.

The theory for the Sverdrup transport also applies to a stratified fluid, by taking a vertical

integral over the planetary vorticity balance relation (Chap. 1),

$$\beta v_g \approx f \frac{\partial w}{\partial z}, \tag{21}$$

where the resulting right-hand-side can then be related to the Ekman pumping at the top of the ocean interior and a depth integral can be taken to relate the curl of the surface stress to the meridional transport. However, when the Taylor-Proudman theorem does not hold for the interior flow between the top and bottom boundary layers — as here because of the stratification — then (21) cannot be easily interpreted to determine the vertical profile of the gyre circulation.

3.1   Layered, Quasigeostrophic Models

We will solve the QG equations (Chap. 1) for the baroclinic wind-gyre problem. This has the particular advantage that the basic stratification is specified independently from the circulation dynamics, and it allows a simplifying adiabatic approximation for the latter. We assume there is a rotating, stably stratified environment, with the respective frequencies, $f(y) = f_o + \beta y$ and $N(z) = \sqrt{d\bar{b}/dz}$. The currents, pressure, and buoyancy fluctuations in this environment satisfy the 3D continuity relation and the QG vorticity, hydrostatic, and buoyancy equations, respectively:

$$
\begin{aligned}
\frac{D}{Dt_g}[\zeta + f(y)] &= f_o w_z + [\nu_v \zeta_z]_z + \nu_h \nabla_h^2 \zeta \\
f_o \psi_z &= b \\
\frac{Db}{Dt_g} + N^2 w &= \kappa_h \nabla_h^2 b.
\end{aligned}
\tag{22}
$$

The geostrophic advective time derivative is

$$\frac{D}{Dt_g} = \partial_t + \mathbf{u}_h \cdot \boldsymbol{\nabla}_h = \partial_t + J[\psi, \ ] \tag{23}$$

(ν_v, ν_h, κ_h) are vertical and horizontal eddy viscosities and diffusivities. For geometric simplicity we assume the domain is a rectangular volume. This problem posing is approximately what William Holland pioneered (Holland and Lin, 1975; Holland, 1986), and it has proven to be a very popular one for investigating gyre dynamics.

The boundary conditions for this problem are the following:

- No-normal flow at the vertical boundaries,

$$
\begin{aligned}
w &= 0 \quad \text{at } z = -H, 0 \\
\Rightarrow \psi_z &= 0 \quad \text{at } z = -H, 0.
\end{aligned}
\tag{24}
$$

- Wind stress at the top surface and Ekman drag at the bottom (with an implicit assumption that these layers are vanishingly thin, *e.g.,* they are contained within the first neighboring layer next to the boundaries after vertical discretization; Fig. 10),

$$
\begin{aligned}
\nu_v \zeta_z &= \operatorname{curl} \boldsymbol{\tau} \ \ \text{at } z = 0 \\
&= Hr\zeta \ \ \text{at } z = -H \, .
\end{aligned}
\tag{25}
$$

- No-normal flow and either no-slip or free-slip stress conditions at the sides.

- Zero buoyancy flux through any of the boundaries (*i.e.,* $\kappa_h b_n = 0$).

Notice that this problem allows the Sverdrup balance in (21), but it also aallows additional dynamical behaviors.

If $\kappa_h = 0$ everywhere, we say the dynamics are adiabatic, since the buoyancy equation in (22) then conserves the fluctuation b along horizontal trajectories. Because $\bar{b}(z)$ is assumed to be independent of time in the QG approximation, the effect of the surface buoyancy fluxes in the real ocean is implicit in the existence of this mean stratification profile — presumed to be established through the thermohaline circulation — whether or not the fluctuation dynamics are diabatic due to $\kappa_h \neq 0$ (which cannot alter the horizontally averaged value of b, and so might still be called quasi-adiabatic). It would, however, be inconsistent to have $\kappa_v \neq 0$ in this QG approximation, because that would necessarily imply a diabatic evolution of $\bar{b}(z)$, though it could be very slow if κ_v were very small (as in the oceanic interior). This view of the wind-driven circulation as essentially adiabatic (or quasi-adiabatic) can be meaningful only over short time scales compared to the evolution of the thermohaline circulation over many decades or centuries. It also assumes their dynamics are mutually independent; this is not likely to be strictly valid for nonlinear solutions (*n.b.,* we further consider their combination in Chap. 7).

We can combine the component equations in (22) into the QG potential vorticity equation with combined effects from the several types of eddy diffusion,

$$
\frac{Dq}{Dt_g} = \left([\nu_v + (\frac{f_o}{N})^2 \kappa_h]\zeta_z \right)_z + \nu_h \nabla_h^2 \zeta \, ,
\tag{26}
$$

where $\zeta = \nabla_h^2 \psi$ and

$$
q = \beta y + \zeta + f_0^2 \left(\frac{\psi_z}{N^2(z)} \right)_z \, .
\tag{27}
$$

Note that a vertical integral of (26)-(27), using the boundary conditions (24)-(25), would recover the barotropic equation (13), in all terms except for the nonlinear advection that would have an additional quadratic product of the baroclinic components. Insofar as the latter is of consequence — as it usually is — the barotropic components of the solutions of these two models will not generally be the same.

9

We construct a vertical discretization of (22)-(27) into $M \geq 2$ vertical layers. One can view this as a simplifying physical approximation based on the impression, by some, that the oceanic stratification and currents often have their strongest gradients concentrated at interfaces between somewhat homogeneous water masses, or one can view it as a computational necessity for solving the model equations numerically, along with further discretizations in (x, y, t). The most natural indexing scheme of vertical discretization is indicated in Fig. 10, where the goal of having spatially compact finite difference operators leads to a staggering where the variables (ψ, ζ, q) and the associated (vorticity, potential vorticity) equations are located in the middle of the layers, but the variables (b, w) and the (hydrostatic, buoyancy) equations are located at the interfaces.

Now consider what can be called *the dilemma of surface confinement*. The preceding equations have the following property: if we make the combined assumptions of

(a) $\kappa_h = 0$ (adiabatic)

(b) $\nu_v = 0$ (weak vertical mixing outside the PBL)

(c) $\partial_t = 0$ (steady solution),

then we can show that the vertically discretized QG model must have its circulation confined to the top model layer. In this solution (ζ_1, ψ_1) satisfy the equation,

$$J[\psi_1, \zeta_1 + \beta y] = \frac{1}{h_1}\mathrm{curl}\,\tau + \nu_h \nabla_h^2 \zeta_1 \tag{28}$$

since the Jacobian of ψ_1 and the vortex stretching term in q_1, proportional to ψ_1 here, vanishes. The first interfacial buoyancy is linearly proportional to ψ_1,

$$b_1 = f_o \psi_1 / \hat{h}_1 \tag{29}$$

(where $\hat{h}_j = \frac{1}{2}(h_{i=j} + h_{i=j+1})$ is the vertical thickness associated with the interface j). The first interfacial vertical velocity vanishes,

$$w_1 = -\frac{f_o}{N_1^2}J[\frac{1}{2}(\psi_{i=1} + \psi_{i=2}), b_1] \propto J[\psi_1, \psi_1] = 0 \tag{30}$$

(where $N_j^2 = \Delta \bar{b}_j / \hat{h}_j$). All other dependent variables are zero,

$$\psi_i = \zeta_i = 0 \;\forall\, i \geq 2, \quad w_j = b_j = 0 \;\forall\, j \geq 2. \tag{31}$$

Note that this solution is equivalent to the nonlinear, barotropic potential vorticity equation (13), except that here it applies to a flow confined to a possibly very thin layer next to the upper surface. In the limit where $M \to \infty$, putatively approaching a continuously stratified fluid where $h_1 \to 0$ and $\psi_1, \zeta_1 \to \infty$. Thus, there is a singularity of surface confinement of the steady circulation.

Of course, the real ocean is not in this surface-confined state. What is wrong with the previous solution? Among its several approximations, the greatest falseness is in the assumption (c) that the

solution is steady. When a 3D gyre circulation pattern becomes strongly surface trapped, it develops a large vertical shear and is thus susceptible to a baroclinic instability that generates mesoscale eddies with rectification effects that alter the preceding balances. This type of rectification is referred to as *isopycnal form stress*.

3.2   Isopycnal Form Stress

In an adiabatic fluid, an isopycnal surface is a material one, and fluid cannot move across it. In the QG limit this surface is effectively a level one, so the corresponding statement is that fluid does not move between separate layers at different z values. It is well known from aeronautics that there can be an integrated pressure force exerted on a material surface. The same is true here, except the surface is an undulating isopycnal instead of a rigid airplane wing.

Figure 11 illustrates the geometry of an isopycnal with a vertical displacement, $\eta(x, y, z, t) = -\frac{f_o}{N^2}\psi_z$, around its mean level and the corresponding form stress,

$$
\begin{aligned}
D^{(x)} &= \overline{\phi\eta_x(x,y)} \\
&= -\overline{\phi_x\eta} \\
&= -f_o\overline{v\eta} \\
&= \frac{f_o^2}{N^2}\overline{\psi_x\psi_z}\,,
\end{aligned}
\tag{32}
$$

that is the integrated pressure force in the x direction acting on the isopycnal surface, $z = -H_0 + \eta$ (with H_0 its mean depth). Using geostrophic, hydrostatic relations we can rewrite (32) as

$$
D^{(x)} = \frac{f_o}{N^2}\overline{vb}\,,
\tag{33}
$$

and see that it is equivalent to a horizontal eddy buoyancy flux. The form stress contributes to a layer-integrated momentum balance in the following way:

$$
\frac{\partial}{\partial t}\overline{h\mathbf{u}_h} = \dots - h_o\overline{\frac{\partial\eta}{\partial z}\boldsymbol{\nabla}_h\phi} = \dots + h_o\frac{\partial}{\partial z}\mathbf{D}\,,
\tag{34}
$$

since $h = h_o[1 + \partial\eta/\partial z]$. (We use a convention of denoting additional, but here unspecified, terms in the equation by the repeated dots.) Thus, $\mathbf{D}$ acts as an eddy vertical flux of horizontal momentum, as expected from its definition as the integrated force against the material surface — the density interface (or pycnocline) — that vertically separates the different fluid layers.

We can see that the existence of $\mathbf{D} \neq 0$ breaks the surface confinement by forcing a nonzero

time-averaged vertical circulation,

$$
\begin{aligned}
\overline{w} &= \quad\dots - \frac{1}{N^2}\overline{J[\psi', b']} \\
&= \quad\dots - \frac{f_o}{N^2}\overline{\boldsymbol{\nabla}\cdot[\hat{z}\times\boldsymbol{\nabla}\psi']\,\psi'_z} \\
&= \quad\dots + \frac{f_o}{N^2}\hat{z}\cdot\overline{\boldsymbol{\nabla}\times[\psi'\,\psi'_z]} \\
&= \quad\dots + \frac{1}{f_o}\hat{z}\cdot\boldsymbol{\nabla}\times\mathbf{D}\,. \quad (35)
\end{aligned}
$$

In particular, $\overline{w}_1 \neq 0$.

If we chose to parameterize these eddy fluxes of buoyancy and momentum as eddy diffusion processes, then we see that they would correspond to the diffusion terms in (22) with coefficients κ_h and ν_v, respectively. Thus, we see several ways of resolving the dilemma of surface confinement — by relaxing any of the assumptions (a), (b), and (c) — that are all physically equivalent. Either the transient rectification by the eddies must be resolved in a calculation of the unstable equilibrium circulation or it must be parameterized in a calculation of a possibly steady and stable circulation with eddy diffusion terms intended to represent the same dynamical process.

In particular, note that ν_v and κ_h contribute to the composite potential vorticity dynamics in (26) exactly the same way if their values are related by

$$
\nu_v^{equiv} = \frac{f_o^2}{N^2}\kappa_h\,. \quad (36)
$$

The superscript here is meant to indicate that κ_h can reasonably be viewed as the more fundamentally meaningful parameterization of the isopycnal form stress. It is an eddy-diffusion representation of the buoyancy flux, $\overline{\mathbf{u}'_h b'}$,

$$
\kappa_h\nabla_h\overline{b} = -\overline{\mathbf{u}'_h b'}\,; \quad (37)
$$

whereas ν_v^{equiv} is not an eddy diffusion representation of the eddy Reynolds stress $\overline{w'\mathbf{u}'_h}$ (which is too small to contribute at leading order in Ro in QG theory), but rather it is an indirect consequence of the geostrophic equivalence of form stress and buoyancy flux above that can be expressed as

$$
\nu_v^{equiv}\overline{\zeta}_z = \hat{z}\cdot\boldsymbol{\nabla}\times\mathbf{D}\,. \quad (38)
$$

Observations suggest that $\kappa_h \sim 10^3$ m^2 s^{-1} in the ocean (*cf.*, the float dispersal diffusivity in Chap. 1 and the inferred eddy-viscosity values for the Munk solution in Sec. 1). This implies a $\nu_v^{equiv} \sim 10^0$ m^2 s^{-1} for $f_o = 10^{-4}$ s^{-1} and $N = 3 \times 10^{-3}$ s^{-1} (*i.e.*, $2\pi/N = 2000$ s $= 0.5$ hr). In contrast estimates of ν_v from vertical Reynolds stresses associated with small-scale, shear-flow turbulence (*e.g.*, Kelvin-Helmholtz instability) indicate that values of ν_v are about 10^{-3} m^2 s^{-1} or smaller outside of the PBL, and they are very much smaller than the ν_v^{equiv} above. Another way to interpret this value of ν_v^{equiv} is that it allows $\nu_v^{equiv}\cdot\partial\overline{\mathbf{u}}/\partial z$ to have the same order of magnitude

12

as $\tau \sim 10^{-4}$ m^2 s^{-2} for a typical large-scale vertical shear across the pycnocline of $\partial \overline{\mathbf{u}}/\partial z \sim 0.1$ m s^{-1} / 10^3 m = 10^{-4} s^{-1}. That is, the magnitudes of the interior and surface wind stresses are similar, consistent with there being a significant downward momentum flux into the interior.

In summary, the vertical penetration of the wind-driven gyres in the ocean is regulated primarily by eddy rectification due to isopycnal form stress. Typically the horizontally broad currents in these gyres are mostly contained within and above the main pycnocline, (*i.e.,* within the top 1 km; *e.g.,* the solutions below). In OGCMs with coarse grids that do not resolve the mesoscale instabilities, this effect has usually been parameterized by κ_h or some alternative with similar effects (*e.g.,* the quasi-adiabatic eddy transport parameterization of Gent and McWilliams (1990) described in the next section that reduces to a κ_h form in the QG limit).

3.3 Eddy-Driven Transport Velocity

Closely related to the isopycnal form stress is an eddy-induced mass transport (a.k.a. *bolus velocity*), analogous to the Lagrangian mean flow (*i.e.,* Stokes drift) for surface gravity waves. The Stokes-drift effect in wave-averaged dynamics was derived rigorously with the assumptions of a small wave slope and a clear separation of time scale between surface waves and currents (Chap. 2). There is an advective effect on circulation dynamics averaged over mesoscale eddies (*i.e.,* over scales of ~ 100 km and/or months), such that the evolution equation for a mean tracer field has a form,

$$\frac{\partial \overline{c}}{\partial t} \; = \; ... \; - \mathbf{u}^* \cdot \boldsymbol{\nabla} \overline{c}, \tag{39}$$

where

$$\mathbf{u}_h^* \; = \; \overline{\partial_b \eta' \mathbf{u}_h'}/\partial_b \overline{\eta}, \quad w^* \; = \; -\int^z \boldsymbol{\nabla} \cdot \mathbf{u}_h^* \, dz. \tag{40}$$

Here $\mathbf{u}^*$ is the eddy-driven transport velocity that is an increment to the mean tracer advection by the mean velocity (*i.e.,* it is a contribution added to the Eulerian mean flow to obtain the Lagrangian mean flow). The formal definition of $\mathbf{u}^*$ is in terms of eddy mass fluxes. Gent and McWilliams (1990) proposed a parameterized as eddy-diffusion of variations in the thickness of a fluid layer bounded by isopycnals (assuming nearly adiabatic motion in a stably stratified interior region); this leads to

$$\mathbf{u}_h^* \; = \; -[\kappa \mathbf{L}]_z, \quad w^* \; = \; \boldsymbol{\nabla}_h \cdot [\kappa \mathbf{L}], \quad \mathbf{L} \; = \; -\boldsymbol{\nabla}_h \overline{b}/\overline{b}_z. \tag{41}$$

This formula is on a less firm theoretical foundation than (40), both because there is no simple analytic formula for mesoscale eddies that allows an explicit evaluation of $\mathbf{u}^*$ and because there is no clear separation of space and time scales between mesoscale currents and circulation. Nevertheless, (40)-(41) have been shown to have substantial, and seemingly beneficial, influences on circulation solutions in OGCMs. This is further discussed in Chaps. 4 and 7. We will not make use of them in this Chapter because our focus is on equilibrium baroclinic solutions where the eddies, hence their effects on the mean circulation, are explicitly resolved in the calculation.

3.4 Turbulent Equilibrium Solutions

In the nonlinear, baroclinic, transient regime, (26)-(27) must be solved numerically. Here we will examine four different solutions (Berloff and McWilliams, 1999). The solutions have the strongest permissible vertical truncation that allows baroclinicity, with $M = 2$. The domain has dimensions $L_x = L_y = 3840$ km and $H = 4000$ m. The Coriolis frequency is represented by the β-plane approximation, with $f_o = 0.83 \times 10^{-4}$ s^{-1} and $\beta = 2 \times 10^{-11}$ m^{-1} s^{-1}. The mean layer thicknesses are $h_1 = 300$ m and $h_2 = 3700$m. The interfacial buoyancy difference is $\Delta \bar{b}_1 = 0.067$ m s^{-2}, so that the baroclinic deformation radius is

$$R \equiv \sqrt{\frac{\Delta \bar{b}_1 h_1 h_2}{H f_o^2}} = 52 \text{ km.} \qquad (42)$$

The bottom-drag damping rate is $r = 0$, and the solutions are adiabatic, with $\kappa_h = 0$. The values of ν_v and ν_h vary between the cases. The wind stress pattern is

$$\text{curl} \, \boldsymbol{\tau} = \tau_o \frac{\pi}{L_y} \cdot \left(\sin \left[\frac{\pi y}{L_y} \right] - \lambda \cos \left[\frac{\pi y}{2 L_y} \right] \right), \qquad (43)$$

with $\tau_o = 0.5 \times 10^{-4}$ m^2 s^{-2}. The parameter λ expresses the asymmetry of the wind forcing between the gyres. The value $\lambda = 0$ implies equal wind forcing of the subtropical and subpolar gyres, and $\lambda > 0$ implies a stronger forcing of the subtropical gyre, as is generally believed to be true in nature.

Results are shown in Figs. 12-21 from four different solutions:

1. $\nu_h = 1600$ m^2 s^{-1}, $\nu_v = 0$ m^2 s^{-1}, $\lambda = 1$.

2. $\nu_h = 1600$ m^2 s^{-1}, $\nu_v = 0.2$ m^2 s^{-1}, $\lambda = 1$.

3. $\nu_h = 400$ m^2 s^{-1}, $\nu_v = 0$ m^2 s^{-1}, $\lambda = 1$.

4. $\nu_h = 400$ m^2 s^{-1}, $\nu_v = 0$ m^2 s^{-1}, $\lambda = 0$.

These choices imply that solution 1 is steady, stable, and confined to the surface layer; solution 2 is steady, stable, and not confined to the surface layer; and solutions 3 and 4 have unstable mean circulations. Solutions 1-3 have an asymmetric wind forcing, whereas solution 4 has a symmetric wind forcing.

We can consider ν_h and ν_v as control parameters in a bifurcation sequence. For large ν_h and ν_v, the solutions are steady and stable, as in solutions 1 and 2. As ν_h and ν_v decrease, successive instabilities arise, starting with a first transition (as a Hopf bifurcation) from a steady solution to a stable limit cycle (*i.e.,* with fluctuations having only a single period), then moving into a quasi-periodic regime, and then moving into a chaotic regime whose variability exhibits ever broader

band-widths in space and time as the control parameters decrease. Solutions 3 and 4 are in the fully chaotic regime.

Some features to look for in the figures are the following:

- mean and instantaneous ψ_i and q_i patterns

- eddy-driven deep and recirculation zone circulations, and how they differ between the eddy-resolving and eddy-parameterizing solutions

- standing and transient meanders of the separated boundary current, mesoscale eddies, and far-field Rossby wave radiation

- energy time series, frequency spectra, and mean balances (see definitions in Fig. 1)

- time variability of the boundary current separation points

- spontaneous symmetry breaking and metastable (*i.e.,* long-lasting but ultimately non-persistent), multiple equilibria.

These solutions demonstrate that the solution space is quite complex for baroclinic, wind-driven gyres. This is true even with the strong simplifying assumptions made here in Ro and M; in the use of still regrettably large values of ν_h (*i.e.,* not yet achieving sufficiently large Reynolds number to escape doubts about whether these solutions are relevant to the oceanic regime of $Re \gg 1$); in the neglect of buoyancy forcing; and in the idealized shapes of the wind stress and domain. And we must believe that the real ocean is even more complex.

3.5   Potential Vorticity Homogenization

A special topic in oceanic gyre dynamics is the phenomenon of the occurrence of regions of horizontally uniform potential vorticity, at least in in some solutions of (26)-(27). Where this does occur, it provides a great simplification in dynamical interpretation, because the advection in (26) become trivial when $\nabla_h q \approx 0$. It also provides a further constraint on the problem of determining the vertical profile of the circulation; *e.g.,* in a truncation with $M = 2$, the statements that the vertical integral of ψ satisfies the Sverdrup relation and that the lower layer has uniform q suffice to specify $\psi_i(x, y)$ in both layers.

The motivating idea behind homogenization is that the complex parcel trajectories along horizontal surfaces in a field of mesoscale eddies will act mix q until it become spatially uniform whenever there are no competing processes to renew $\nabla_h q$. This is based on the idea that q is a material tracer satisfying an advection-diffusion balance,

$$\frac{Dq}{Dt_g} = \nabla_h \cdot [\kappa \nabla_h q].$$
(44)

15

As discussed in Chap. 1, this type of an advection/eddy-diffusion equation implies that the integrated q-variance cannot increase with time, and in the extreme limit the variance vanishes when q becomes spatially uniform and all the terms are zero individually. In this context, the differences between (26) and (44) are twofold: assumptions are being made that the various non-conservative terms on the right-side of (26) act only to mix q and that the advecting velocity, $\mathbf{u}_h = \hat{z} \times \boldsymbol{\nabla}_h \psi$, is considered to be known independently of $q(x, y, t)$, without necessarily satisfying (27) (*i.e.,* q is a passive tracer). Obviously, these are bold assumptions, but we now see where they lead.

Batchelor (1956) proved what is called the Prandtl-Batchelor theorem: given a steady $\overline{\psi}(x, y)$, then the solution of (44) for any $\kappa(x, y) > 0$ approaches constant q within any closed streamline in the double limit $t \to \infty$ as $\kappa \to 0$. This is proved simply by integrating (44) over the area within $\overline{\psi}(x, y) = \psi_*$ and noting that the advective term cancels out (*cf.,* , the circulation integral (17)). Thus, in steady state, the integral balance is

$$\oint_{\psi_*} \kappa q_n \, ds \;=\; 0\,. \tag{45}$$

Furthermore, if κ is small, then the local balance in (44) is $J[\psi, q] \;\approx\; 0$, hence $q \;\approx\; Q[\psi]$, so that $q_n \;\approx\; dQ/\psi \, \psi_n$. Since ψ_n is everywhere of the same sign along a closed streamline, q_n is also single-signed. Since the integral above requires the weighted average of q_n to be zero, the only consistent distribution is $q_n = 0$. Hence $Q[\psi] = Q_o$, a constant. The time for this to occur in a region of size L is shorter than the diffusion time, $t_\kappa \;\equiv\; L^2/\kappa$, because the recirculating flow sharpens q gradients across streamlines wherever there are variations of q along ψ contours. This is referred to as *shear-enhanced diffusion*, and its time scale can be estimated as $P^{-2/3} t_\kappa$, where $P = VL/\kappa$ is the Peclet number, here assumed to be large (*cf.,* , the Reynolds number, $Re = VL/\nu$). The outcome of shear-enhanced diffusion is a non-trivial distribution $Q[\psi]$; thereafter, any further progress towards homogenization must occur on the slower time scale t_κ.

Figure 22 shows solutions of (44) with spatially uniform κ_o and several different values for P. The flow configuration is an isolated region of recirculating flow — a single eddy or gyre — and the initial tracer distribution is $q(x, y, 0) \;=\; \gamma x$. The homogenization outcome is not a general one since q gradients can continue to be supplied from the persistent gradient outside the gyre; nevertheless, for large P, the late-time distribution becomes well homogenized.

It turns out to be a very subtle question when the preceding model is the dominant dynamical behavior for solutions of (26)-(27). One obvious exception to the assumptions behind (44) is the wind forcing that acts to generate q gradients rather than to mix them away; another exception occurs near boundaries where lateral stresses imply potential vorticity fluxes (that sustain gradients) through the boundary. So, the likelihood of homogenization is diminished in the directly forced layer near the surface (*i.e.,* $m = 1$) and in barotropic solutions where the wind-driving appears in the only potential vorticity equation (but note the modest manifestation of homogenization in the recirculation zone in the barotropic solution of Fig. 6). Since homogenization is favored for large P, we expect it to more likely occur in regions of strong, recirculating flow, *e.g.,* in the vicinity of the inertial, separated western boundary current. Conversely, it is less likely to occur away from the recirculation zone, both horizontally and vertically, because the mean flow is relatively weaker;

nor near the bottom (*i.e., $m = M$*) if the non-diffusive bottom drag rate r is large enough; nor near the horizontal boundary if the boundary conditions are not consistent with uniform q, especially in the west where solution gradients are largest near the boundary. Finally, there is also no guarantee that either mesoscale rectification or the $(\nu_v,\ \nu_h,\ \kappa_h)$ terms in (26) will act in a laterally diffusive way on q, as in (44), although for them to do so would be consistent with the common paradigm of eddy rectification as mixing.

There is also something of a paradox in the arguments about homogenization. In the passive scalar problem (44), homogenization is expected in the limit $\kappa \to 0,\ P \to \infty$ that one would tend to associate with weak eddy diffusion. However, in the "active" scalar problem where ψ and q are related, we should only expect homogenization where the eddies are at least strong enough to mix away the spatial variations in the background planetary component of q, *viz.,* βy. We can estimate the size of eddy potential vorticity fluctuations δq by an argument of Lagrangian conservation of total q in the presence of a mean gradient $\boldsymbol{\nabla}_h \bar{q}$:

$$\delta q \ \approx \ \boldsymbol{\nabla}_h \bar{q} \cdot \boldsymbol{\delta} \mathbf{x}\,, \tag{46}$$

where $\boldsymbol{\delta}\mathbf{x}$ is the Lagrangian parcel displacement away from its mean location. This approximation is valid on a time scale before the δq anomaly dissipates through its turbulent cascade. Thus, eddy currents must be strong enough, to make $\boldsymbol{\delta}\mathbf{x}$ large enough, to have the capability of making δq large enough to compete with βy variations.

In spite of all these cautionary remarks, there are some spectacular examples of homogenization in solutions of (26)-(27). A first example is Fig. 23 from a $M = 3$ solution with a symmetric, two-gyre wind forcing. Again it is the $m = 2$ layer that is most homogeneous, and this region extends over the greater part of the domain, although there are q gradients around its edges. Note the instantaneous intrusions of tongues of non-uniform $q(x, y, t)$ from around the edges by eddies and the separating western boundary current. Nevertheless, they are so effectively stirred and cascaded to dissipation that they do not penetrate very far into the homogeneous region. (If q' is approximately conserved along trajectories, then it must be small in any large region where $\boldsymbol{\nabla}_h \bar{q}$ is small, because it lacks any sources but still has sinks through advective stirring and diffusion.) Another example, again from a $M = 3$, symmetric two-gyre solution, is shown in Fig. 24: there is no homogenization tendency in the $m = 1$ layer, substantial homogenization for $m = 2$, and only very limited homogenization for $m = M = 3$. Finally, we can also refer to the two solutions in Figs. 14-15 and 18-19 and see that the homogenization in the lower layer is not very strong, in spite of these being cases with $r = 0$ and vigorous deep eddy fields. The degree of homogenization in eddy-resolving baroclinic gyre solutions can also vary substantially as functions of such quantities as the spatial pattern of the wind, the lateral stress boundary condition, the bottom topography, and the magnitude of the sub-mesoscale vertical eddy viscosity ν_v. It is, therefore, still uncertain how much homogenization is to be expected in the real ocean.

The observational evidence for q homogenization in the ocean is mildly supportive, but inconclusive, in my opinion. It is generally a very difficult task to estimate q empirically because of the need to sample the velocity or buoyancy fields in 3D with sufficient accuracy to take the indicated

gradients, although this has been done in a few instances with mesoscale spatial and temporal sampling, as appropriate for use of the QG form of q (and there the result has been that $\boldsymbol{\nabla}_h q \neq 0$). The least difficult form of q to estimate is the planetary potential vorticity, $Q_{pg} = fN^2$, since all it requires is an accurate time average of the vertical profiles of $b(z)$ throughout the region of interest; this can be obtained by hydrographic profiles. This should be an accurate approximation of q if we believe that the mean circulation has very small Rossby number and large horizontal scales (such that ζ is negligible compared to the variations of f or N^2), at least beneath the envelope region of the PBL and away from the western boundary current and recirculation zone. Figure 25 shows observational estimates of $Q(x, y)$ on isopycnal surfaces (relevant for quasi-adiabatic trajectories on large enough spatial scales such that the QG approximation of $b \ll \bar{b}$ is doubtful). These plots suggest that there is indeed a broad region within the main pycnocline of the subtropical gyre in the North Atlantic ocean where Q gradients are small. However, the same argument that justifies $q \approx Q + Ro\,\delta q$ by $Ro \ll 1$, allows the possibility that δq is not necessarily small; hence q variations may be significant at the level of approximation that is represented in our QG model.

4   Gyre Spin-Up and Adjustment

Now consider the time evolution of a wind-gyre towards a steady or turbulent-equilibrium state. The problem can be posed either as the spin-up from rest or as the adjustment to a changing wind stress field. The latter is constantly happening because of atmospheric variability. Variable winds will, of course, force time variation in the circulation, in addition to whatever intrinsic variability is present, but the nature of the response varies with the time scale of the wind fluctuation.

Wind fluctuations on very short time scale give rise to a gravity-wave response (*e.g.,* , similar to tides and tsunamis) that propagate very rapidly across whole basins and reflect and dissipate in shallow water (and perhaps over rough topography), resulting in little circulation change.

On intermediate time scales, the response is primarily as barotropic Rossby waves, and after several basin crossings over several weeks, an altered Sverdrup circulation can be established in the interior, with a vertical current profile that fills the entire depth. This profile leads to an approximate relation between the sea level and the Sverdrup transport streamfunction, $\Psi \approx (gH/f)\,\eta$, where H is the full ocean depth. With this relation a simple phenomenological equation that combines barotropic Rossby waves and Sverdrup circulation is the following:

$$\frac{\partial^3 \eta'}{\partial t \partial^2 x} - \beta \frac{\partial \eta'}{\partial x} = -\frac{f^2}{gH} \, \mathrm{curl}\left[\frac{\boldsymbol{\tau}}{f}\right] . \tag{47}$$

A balance between the right-hand terms yields Rossby wave propagation, with a speed, $c \sim \beta L^2 = \mathcal{O}(20)$ m s^{-1}, where $L = \mathcal{O}(10^3)$ km is the scale of the wind pattern. At the other extreme, a balance neglecting the time derivative yields the Sverdrup transport relation (assuming the geostrophic interior transport is dominant over the Ekman transport). The seasonal cycle is an appropriate time scale for confirming the latter balance, as shown in Fig. 26 for the North Pa-

cific Kuroshio/Oyashio eastward transport, where altimetric η measurements agree with OGCM barotropic transport streamfunction results that are nearly in Sverdrup balance.

On longer time scales, the Sverdrup part of the wind-gyre currents becomes confined in and above the pycnocline, as we have seen in the equilibrium solutions above. The adjustment to this profile from the initially more barotropic one occurs through the propagation of baroclinic Rossby waves with primarily a first-mode vertical structure, in phase throughout the interval from the surface to the pycnocline). Again, after several basin crossing times over a decade or so, the steady-state Sverdrup balance can arise. For a baroclinic profile with nonzero currents above the pycnocline, we can use a different sea-level/transport-streamfunction relation, $\Psi \approx (gH_*/f)\eta$, where H_* is the depth of the pycnocline. This adjustment is represented by the following phenomenological equation:

$$\frac{\partial \eta'}{\partial t} - \beta R^2 \frac{\partial \eta'}{\partial x} = -\frac{f^2 R^2}{gH_*} \operatorname{curl}\left[\frac{\boldsymbol{\tau}'}{f}\right] , \tag{48}$$

where R is the deformation radius for the first baroclinic mode. The right-hand terms imply a long baroclinic Rossby wave speed, $c \sim \beta R^2 = \mathcal{O}(0.02)$ m s^{-1}, where $R = \mathcal{O}(30)$ km. And again, the steady balance is the Sverdrup relation. Decadal variability is an appropriate time scale for this relation to hold, as shown in Fig. 27 for the North Atlantic subtropical gyre: hydrographic η measurements (assuming a level of no motion in the abyss) are fairly well predicted from (48) with forcing by the reanalysis climatology of the Atlantic wind field.

5   Intrinsic Gyre Variability

In addition to gyre variability forced by atmospheric wind fluctuations — begging for now the question of how much the atmospheric variability is a consequence of oceanic variations (Chap. 10) — there is spontaneous low-frequency variability even for steady wind forcing (Berloff and McWilliams, 1999). This is an important phenomenon for both circulation and climate, but as yet it is poorly understood and its magnitude is not well documented from observations (*e.g.,* it is not strongly evident in Figs. 26-27). It seems clear from existing computational examples, however, that interaction among mesoscale eddies, the WBC, and the recirculation zone are primary dynamical ingredients. This is plausible *a priori* since these are the important nonlinear elements of wind-gyre circulation dynamics.

Appendix
QG, M=2

energy $\qquad E(t) = \frac{1}{2} \sum_i \frac{h_i}{H} \langle \nabla \psi_i^2 \rangle + \frac{1}{2H} \frac{f_o^2}{\Delta \overline{b}_1} \langle (\psi_1 - \psi_2)^2 \rangle$

mean
energy $\qquad \overline{E} = \frac{1}{2} \sum_i \frac{h_i}{H} \langle \nabla \overline{\psi}_i^2 \rangle + \frac{1}{2H} \frac{f_o^2}{\Delta \overline{b}_1} \langle (\overline{\psi}_1 - \overline{\psi}_2)^2 \rangle$

eddy
energy $\qquad E' = \frac{1}{2} \sum_i \frac{h_i}{H} \langle \overline{(\nabla \psi_i')^2} \rangle + \frac{1}{2H} \frac{f_o^2}{\Delta \overline{b}_1} \langle \overline{(\psi_1' - \psi_2')^2} \rangle$

mean & eddy
balances $\qquad \dfrac{\partial \overline{E}}{\partial t} = 0 = \overline{W} - H - V - \overline{D}$

$\qquad\qquad\qquad \dfrac{\partial E'}{\partial t} = 0 = H + V - D'$

$\qquad\qquad\qquad \overline{W} = -\frac{h_1}{H} \langle \overline{\psi}_1 \, \text{curl} \, \underline{\uparrow} \rangle$

$\qquad\qquad\qquad \overline{D} = \nu \sum_i \frac{h_i}{H} \langle (\nabla^2 \overline{\psi}_i)^2 \rangle$

$\qquad\qquad\qquad D' = \nu \sum_i \frac{h_i}{H} \langle \overline{(\nabla^2 \psi_i')^2} \rangle$

$\qquad\qquad\qquad H = -\sum_i \frac{h_i}{H} \langle \overline{\nabla \psi_i' \cdot J(\psi_i', \nabla \overline{\psi}_i)} \rangle$

$\qquad\qquad\qquad V = -\frac{f_o^2}{\Delta \overline{b}_1} \langle \overline{(\psi_1' - \psi_2') J(\frac{1}{2}(\psi_1' + \psi_2'), \overline{\psi}_1 - \overline{\psi}_2)} \rangle$
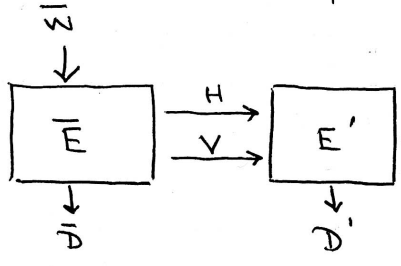
$\overline{\cdot}$ = time average

$\langle \cdot \rangle$ = area average

Figure 1: Appendix: Mean and Eddy Energetics for a 2-Layer, Quasigeostrophic Model.
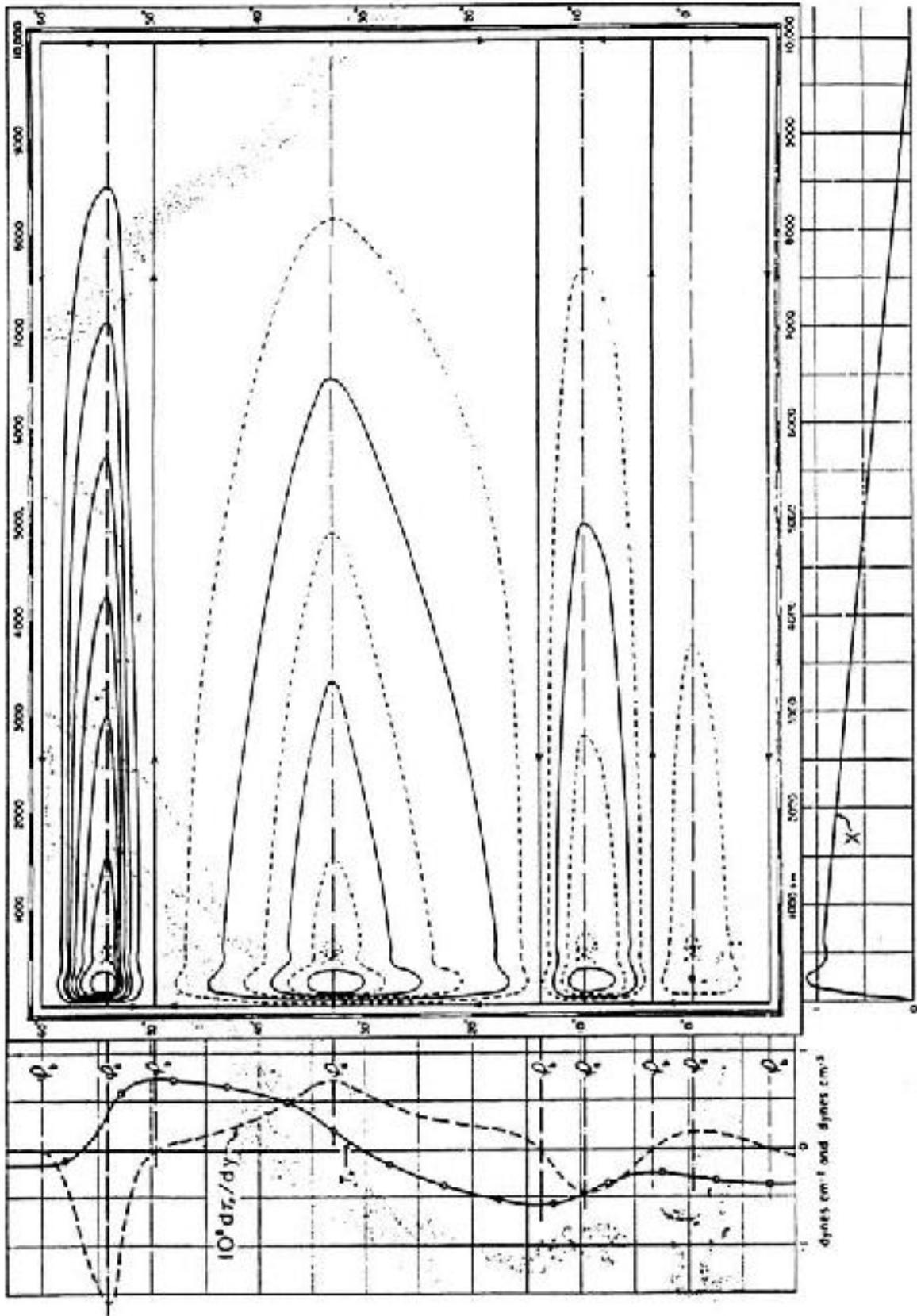
Figure 2: Barotropic streamfunction for the North Pacific, based on the indicated rectangular domain and wind fits (Munk, 1950).

$\psi(x, y)$
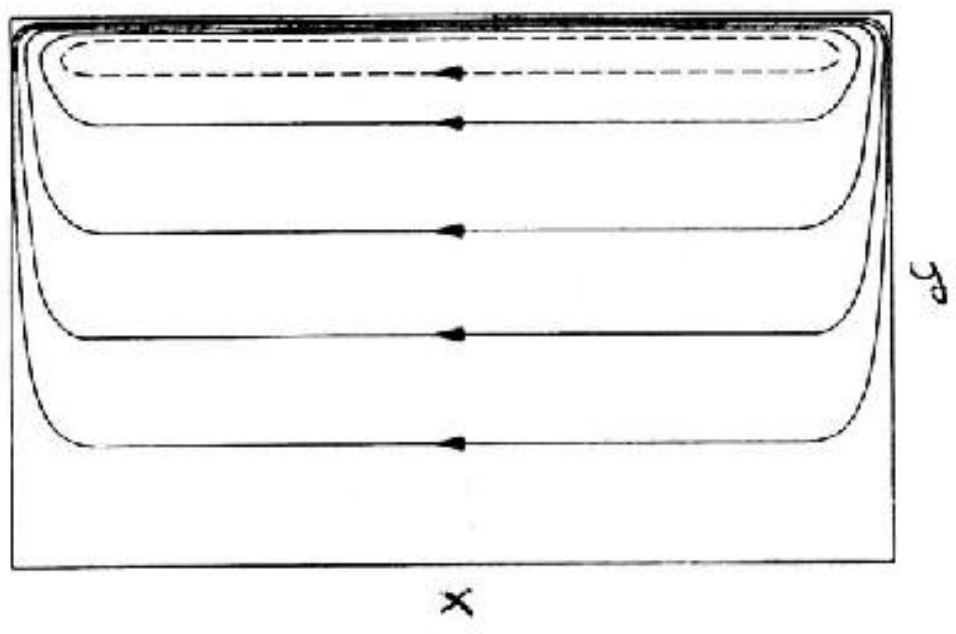
Figure 3: A free inertial solution for a single gyre (Fofonoff, 1954).
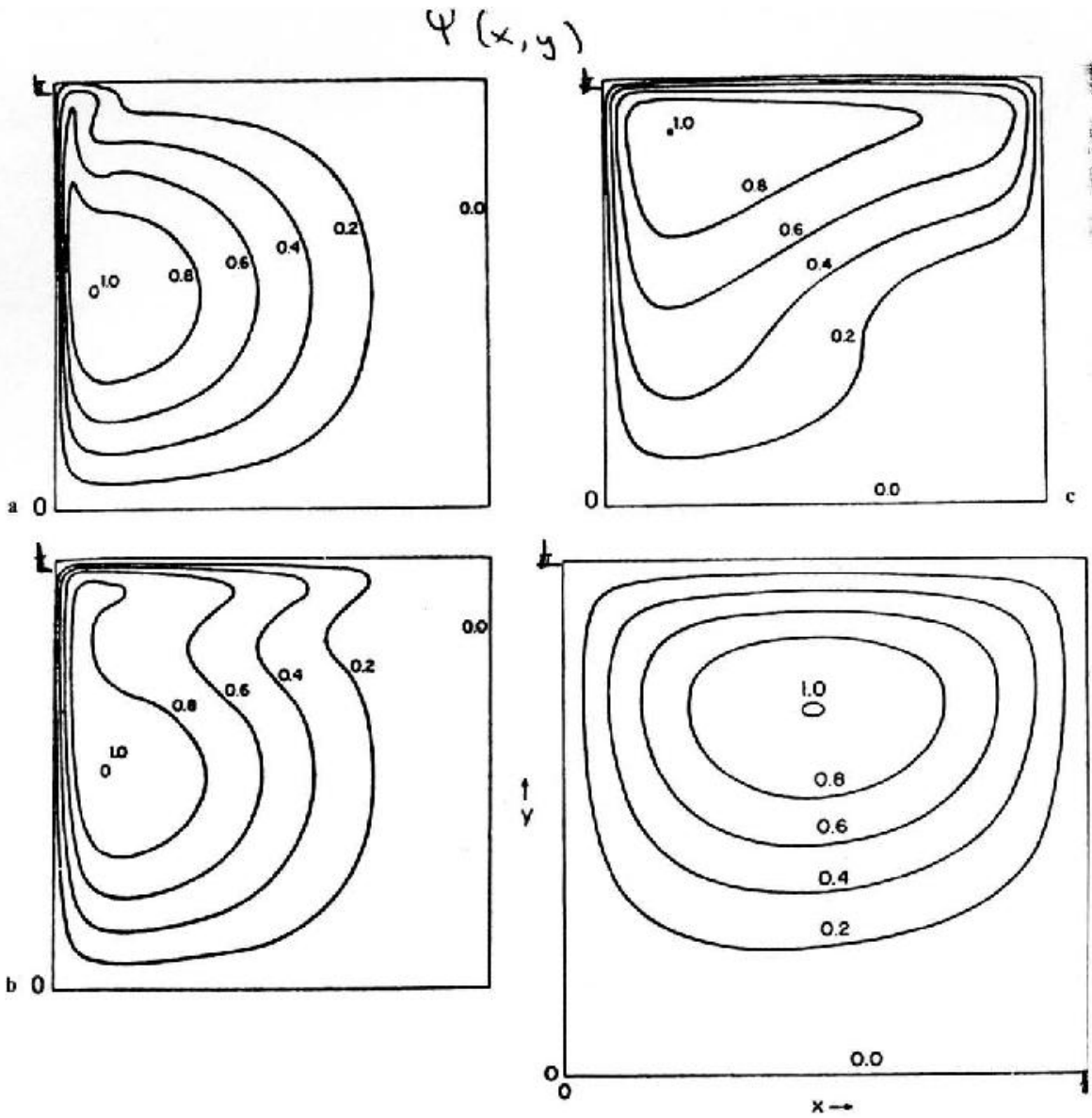
Figure 4: Steady solutions of (13) for a single gyre with bottom friction only (Veronis, 1966). The panels have the following values for δ_c/δ_s: (a) 1, (b) 2, (c) 4, and (d) 8.
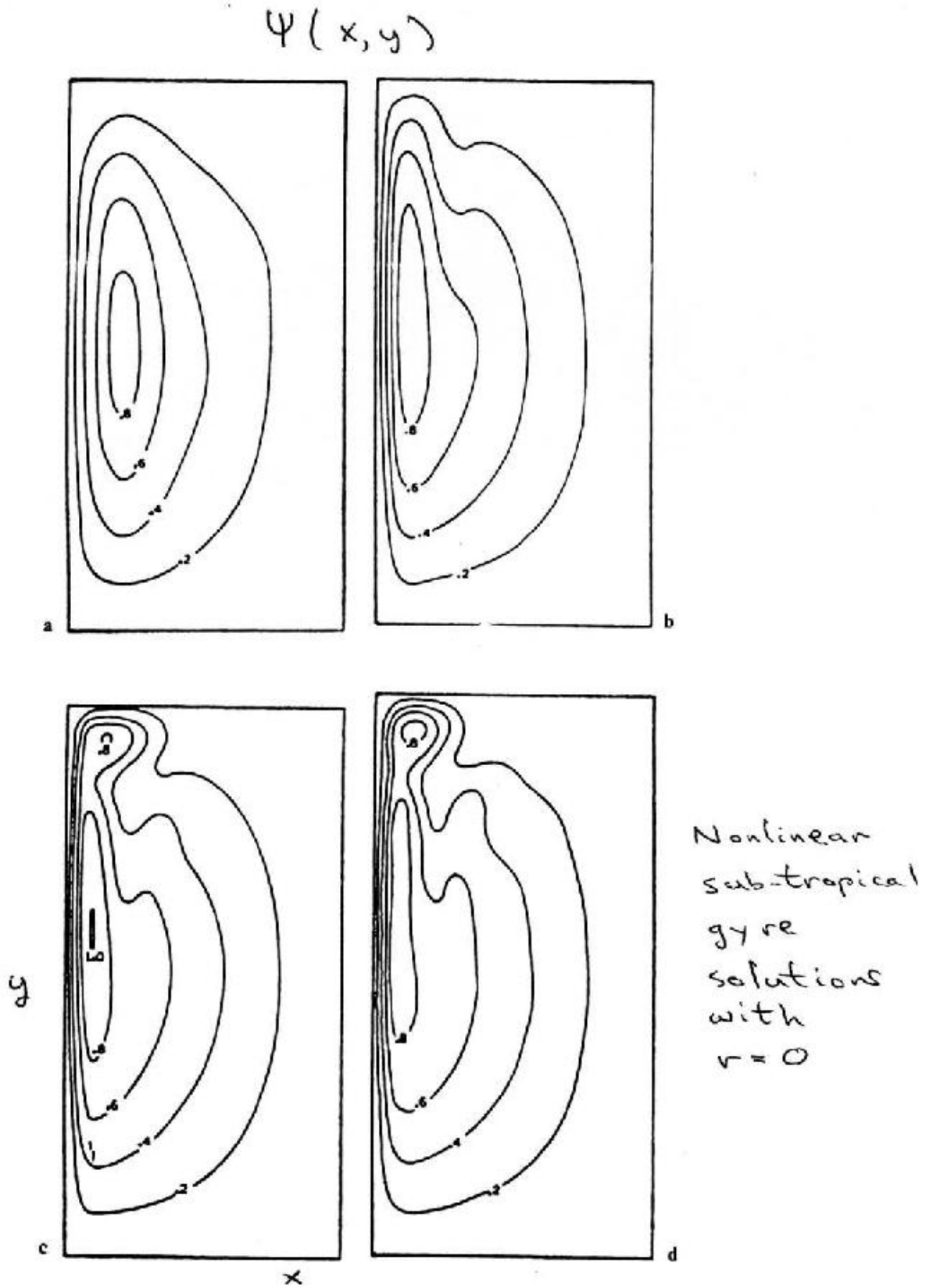
$$\Psi(x, y)$$

Nonlinear
sub-tropical
gyre
solutions
with
$\nu = 0$

Figure 5: Steady solutions of (13) for a single gyre with lateral friction only (Bryan, 1963). The panels have the following values for δ_c/δ_m: (a) 1, (b) 2, (c) 4, and (d) 8.
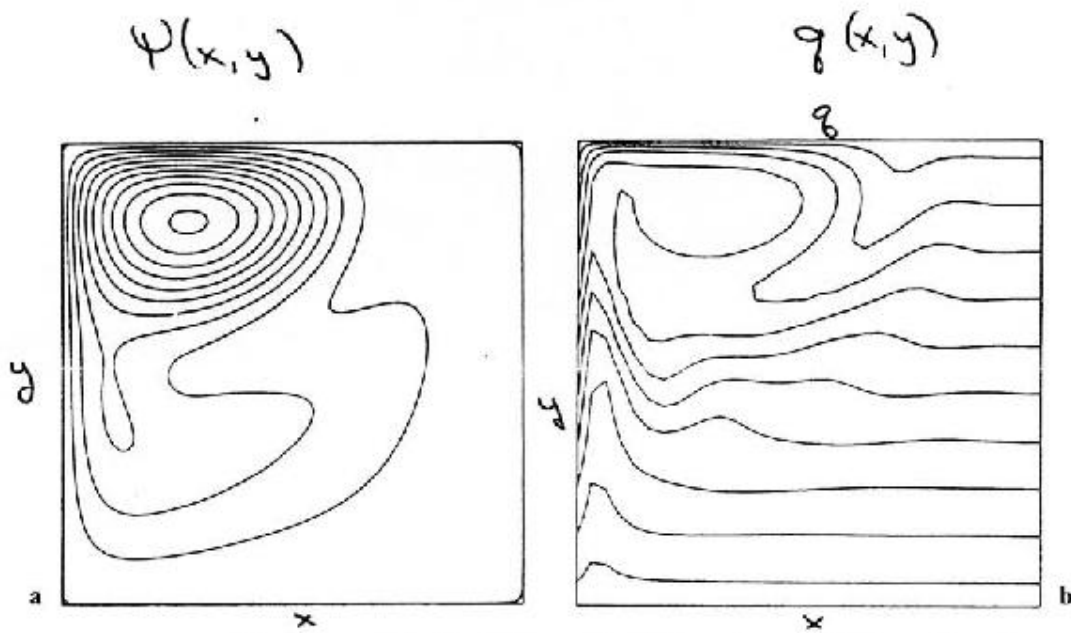
Figure 6: A steady solution of (13) for a single gyre with lateral friction only and a free-slip boundary condition (Böning, 1986). $\delta_c/\delta_m = 1$.
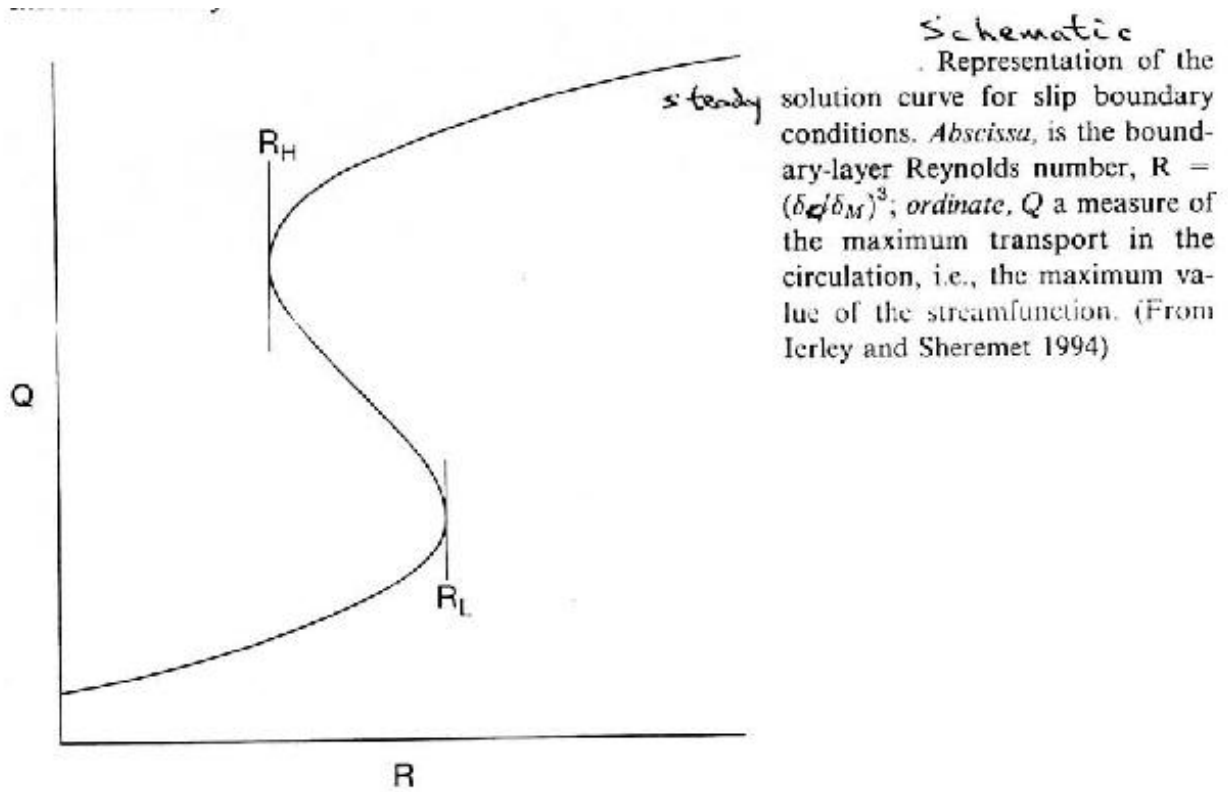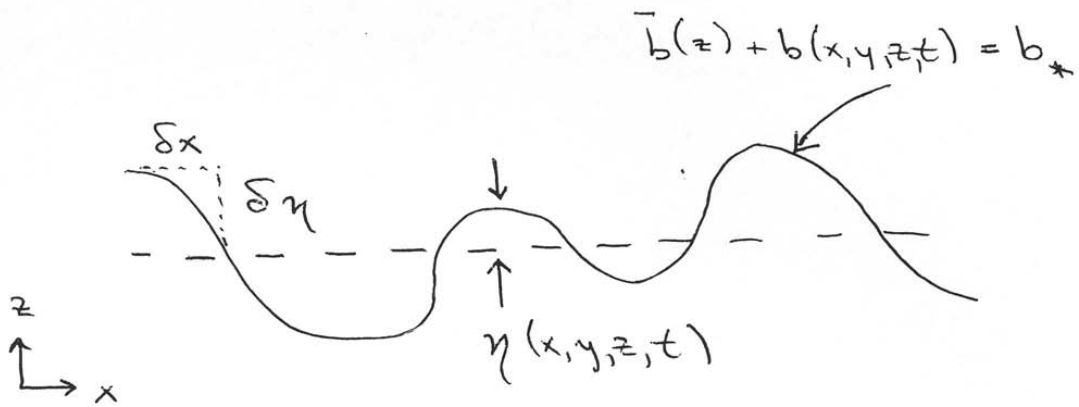
Figure 7: A bifurcation diagram of multiple steady solutions of (13) for a single gyre with lateral friction only and a free-slip boundary condition (Ireley and Sheremet, 1995).

a) $R = 0$ $\max \psi = 1.11$
b) $R = 0.2$ $\max \psi = 1.04$
c) $R = 1$ $\max \psi = 1.66$
d) $R = 1.45$ $\max \psi = 3.55$
e) $R = 2$ $\max \psi = 11.5$
f) $R = \infty$ $\max \psi = 15.1$
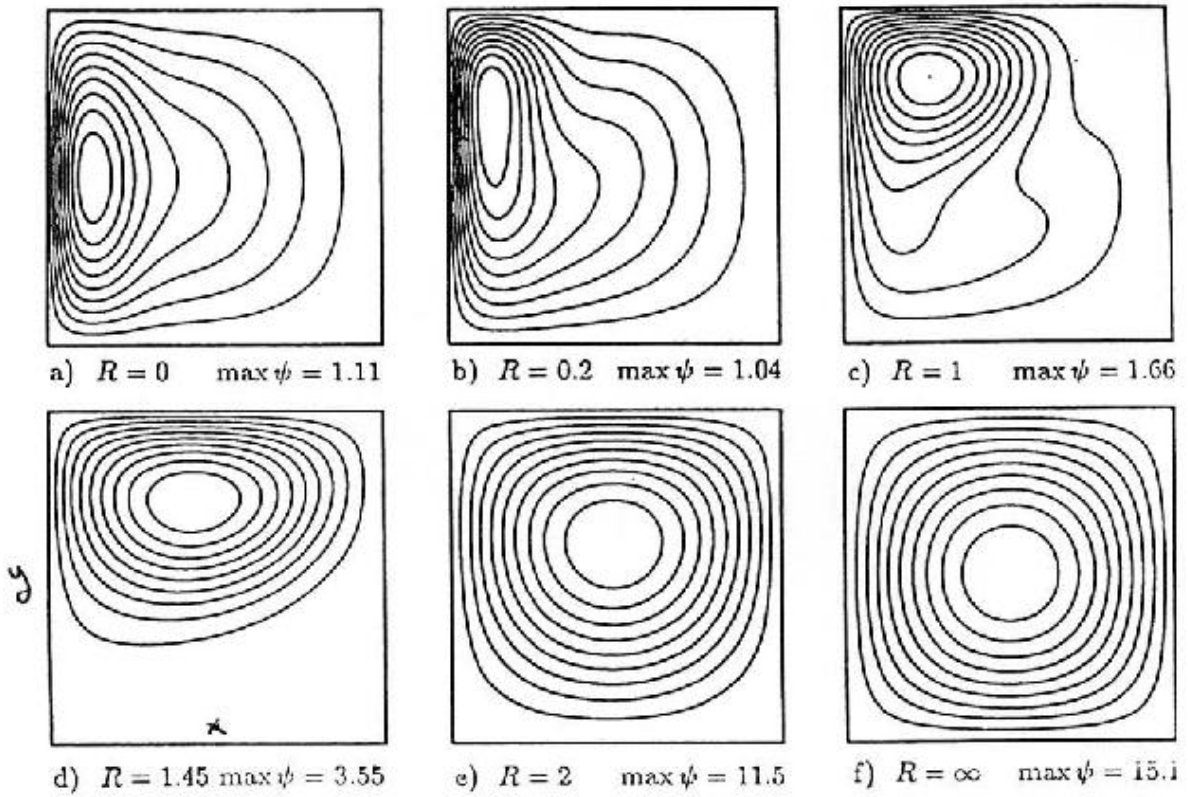
Figure 8: Steady solutions of (13) for a single gyre with lateral friction only and a free-slip boundary condition (Ireley and Sheremet, 1995). Here $R = (\delta_c/\delta_m)^2$.
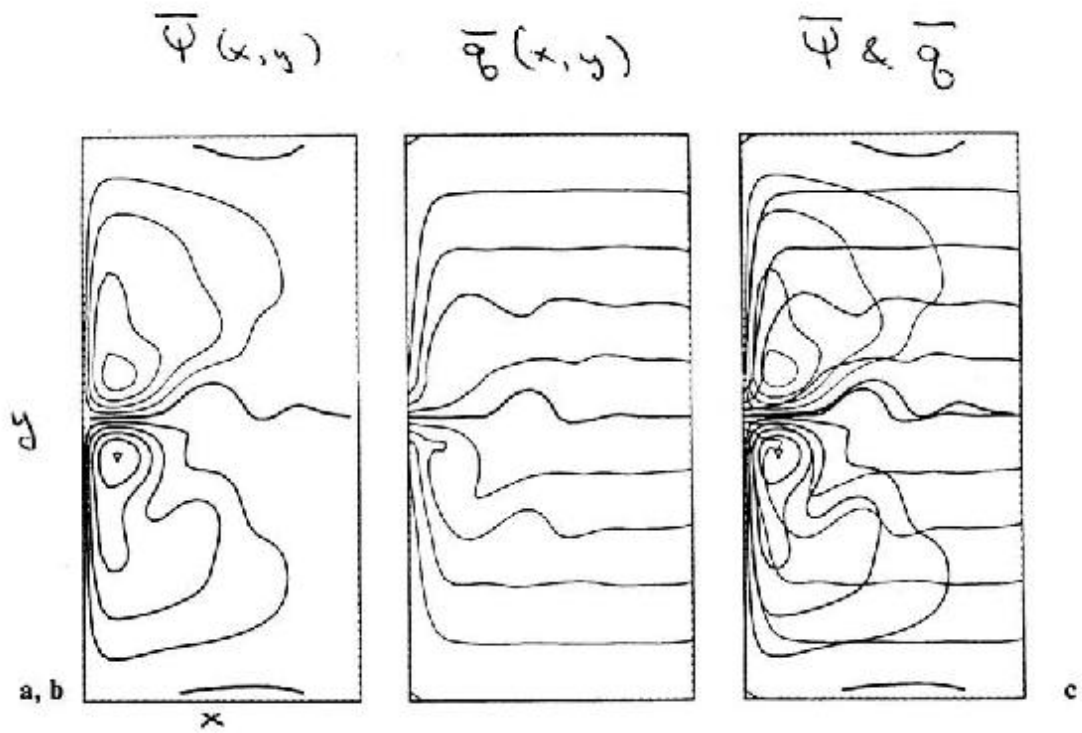
Figure 9: Time-mean fields from a statistically steady solution of (13) for a cyclonic/anticyclonic gyre pair with lateral friction only, $\delta_m \ll \delta_c$, and a free-slip boundary condition (Marshall, 1984).
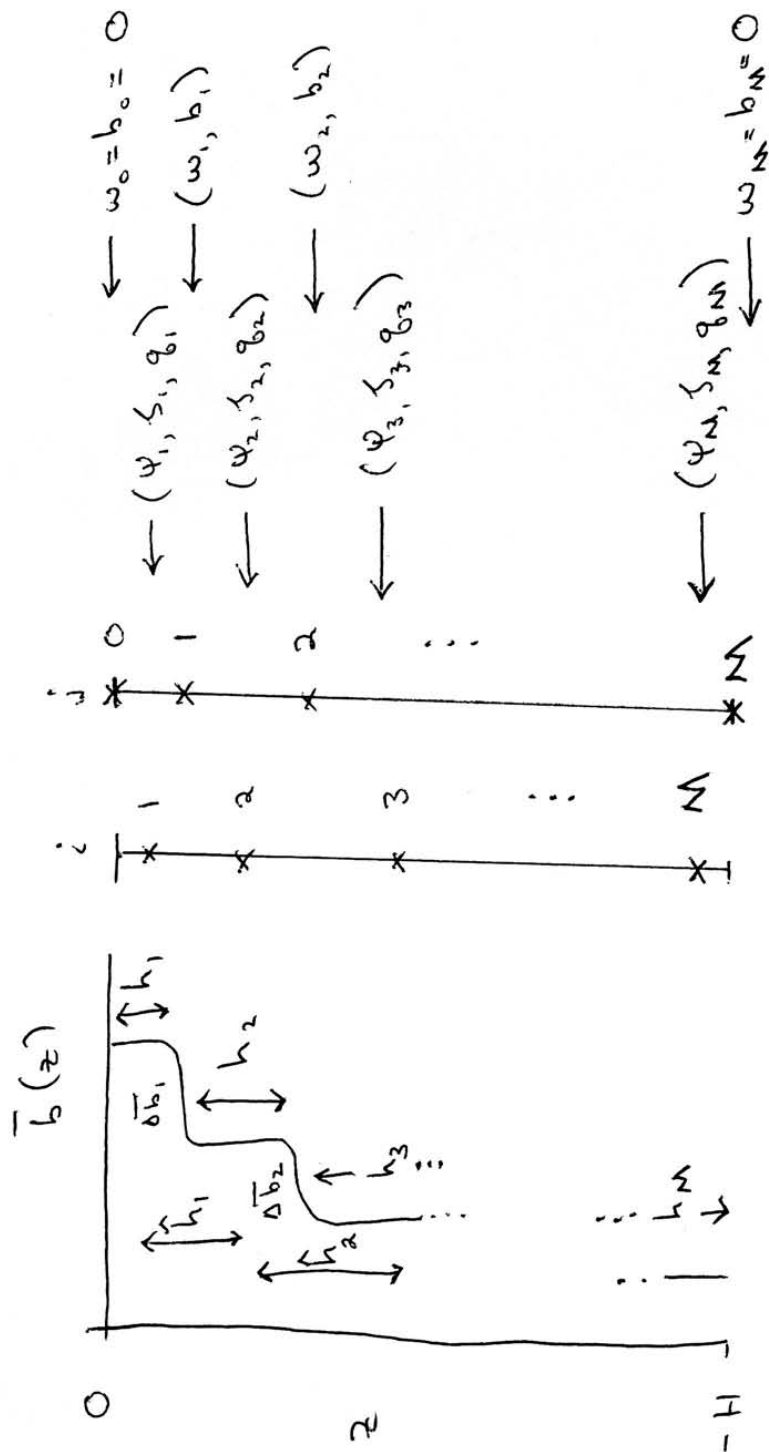
Figure 10: Vertical discretization for a layered, QG model.

$$\overline{b}(z) + b(x,y,z,t) = b_*$$

$$\eta(x,y,z,t)$$

$$\eta = -b/\overline{b}_z \quad \text{if} \quad b << \overline{b}$$

$$\eta = -\frac{f_o}{N^2} \psi_z$$

$$D^{(x)} = \overline{\phi \, \delta\eta/\delta x}^{\,x}$$

$$= -\overline{\delta\phi/\delta x \, \eta}^{\,x} \quad \left(\text{if} \ \overline{\delta(\eta\phi)} = 0 \right)$$

Isopycnal form stress

Figure 11: Isopycnal form stress with the QG approximation.

Upper psi

CONTOUR FROM -120 TO 240 BY 20

Lower psi

CONSTANT FIELD — VALUE IS 0

x

y
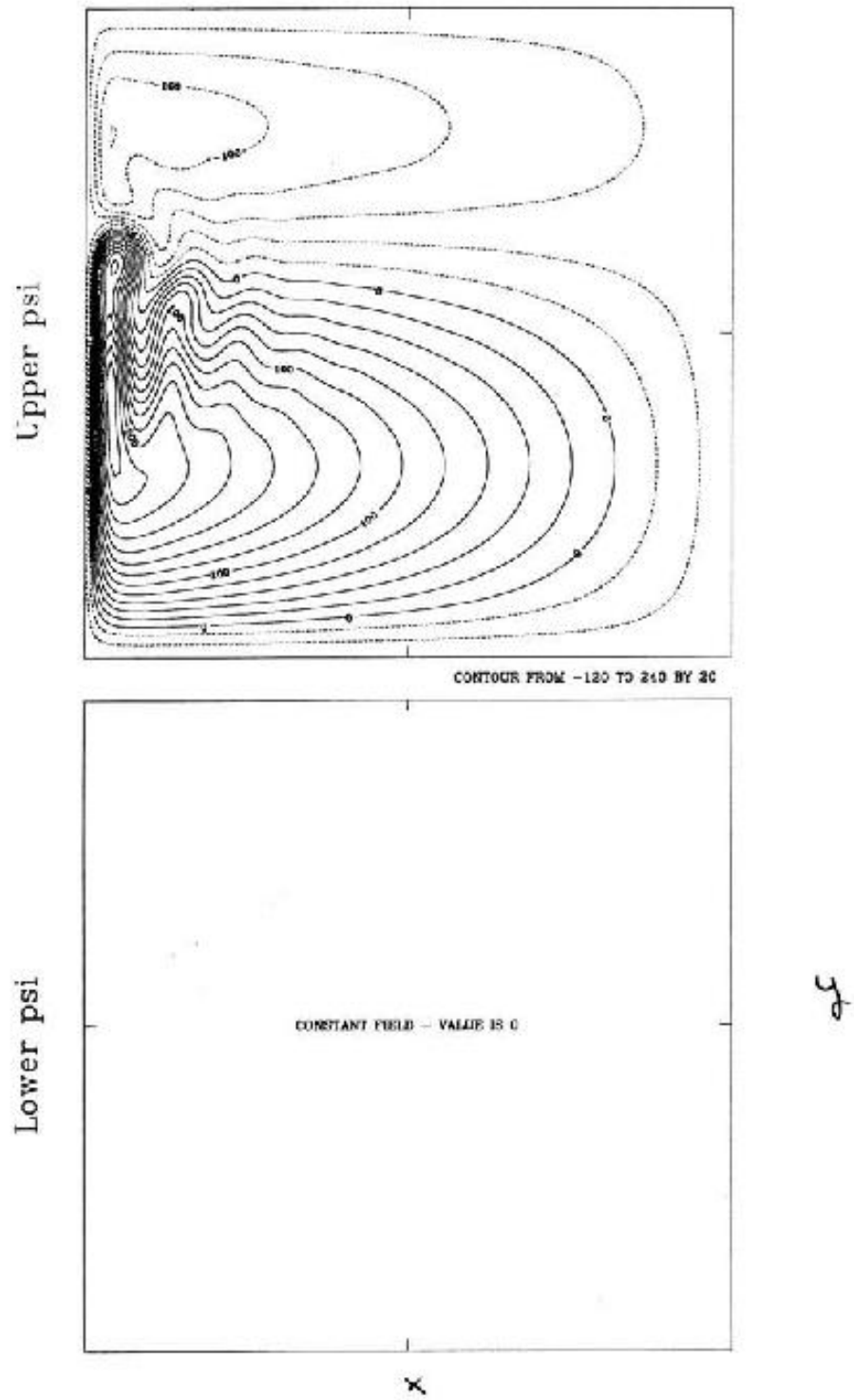
Figure 12: Steady upper-layer streamfunction in solution 1.

Upper psi

CONTOUR FROM -100 TO 220 BY 20

Lower psi

CONTOUR FROM -1.5 TO 3.5 BY .25
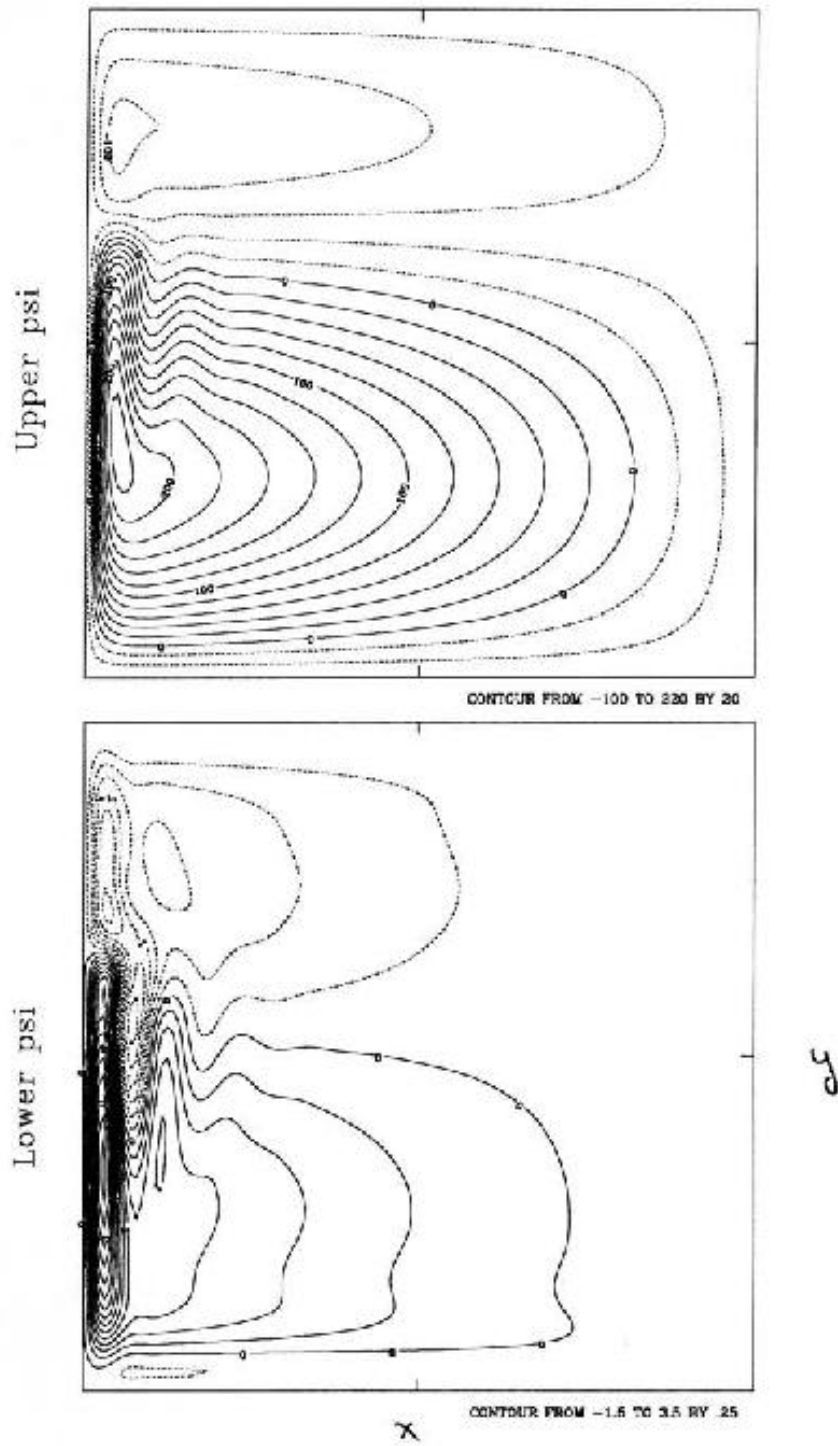
Figure 13: Time-mean streamfunction fields in solution 2.

32

Upper psi

CONTOUR FROM -250 TO 700 BY 50

Lower psi

CONTOUR FROM -25 TO 55 BY 5

Upper PV

CONTOUR FROM -70 TO 180 BY 10

Lower PV

CONTOUR FROM -55 TO 55 BY 5
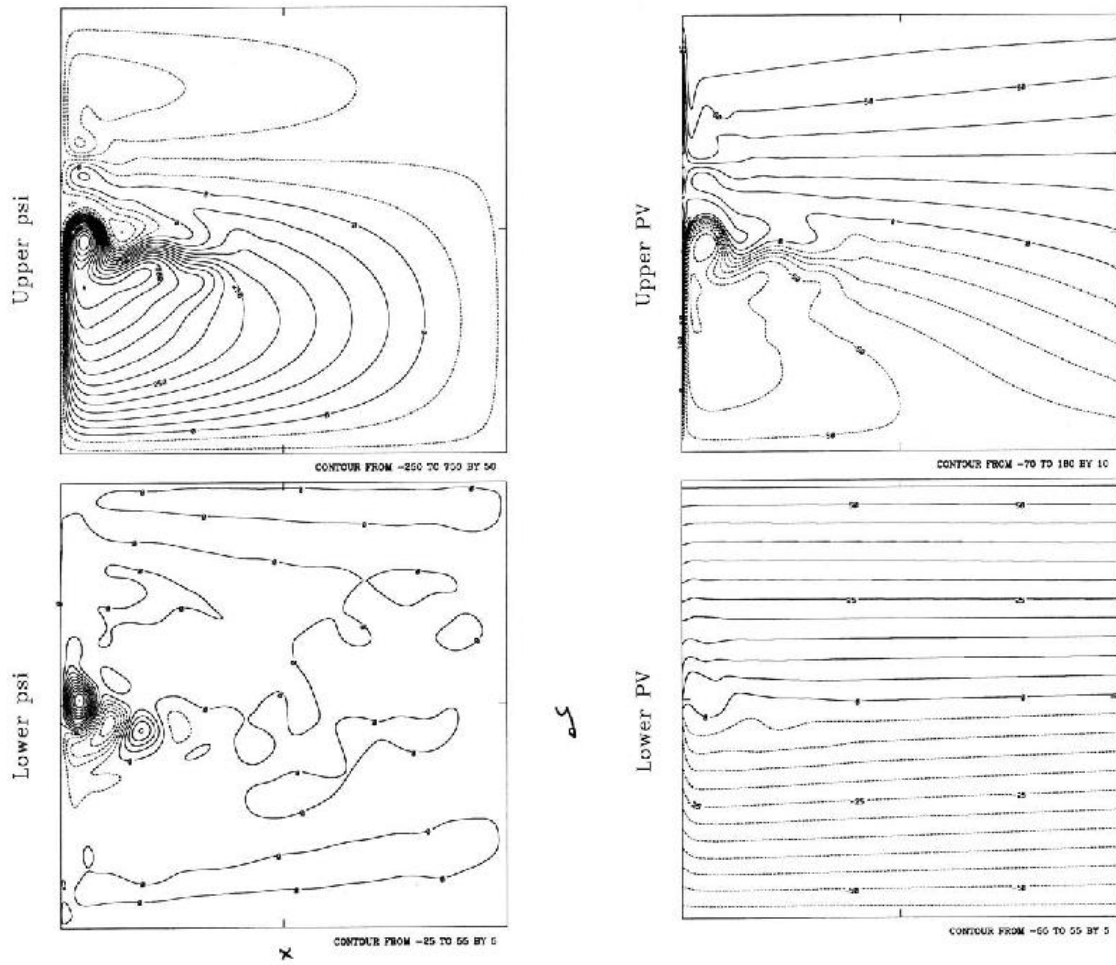
Figure 14: Solution 3: (a) $\overline{\psi}_i$ & (b) $\overline{q}_i$.

Upper psi

CONTOUR FROM -300 TO 800 BY 50

Upper PV

CONTOUR FROM -100 TO 220 BY 20

Lower psi

CONTOUR FROM -90 TO 75 BY 5

Lower PV

CONTOUR FROM -90 TO 55 BY 5
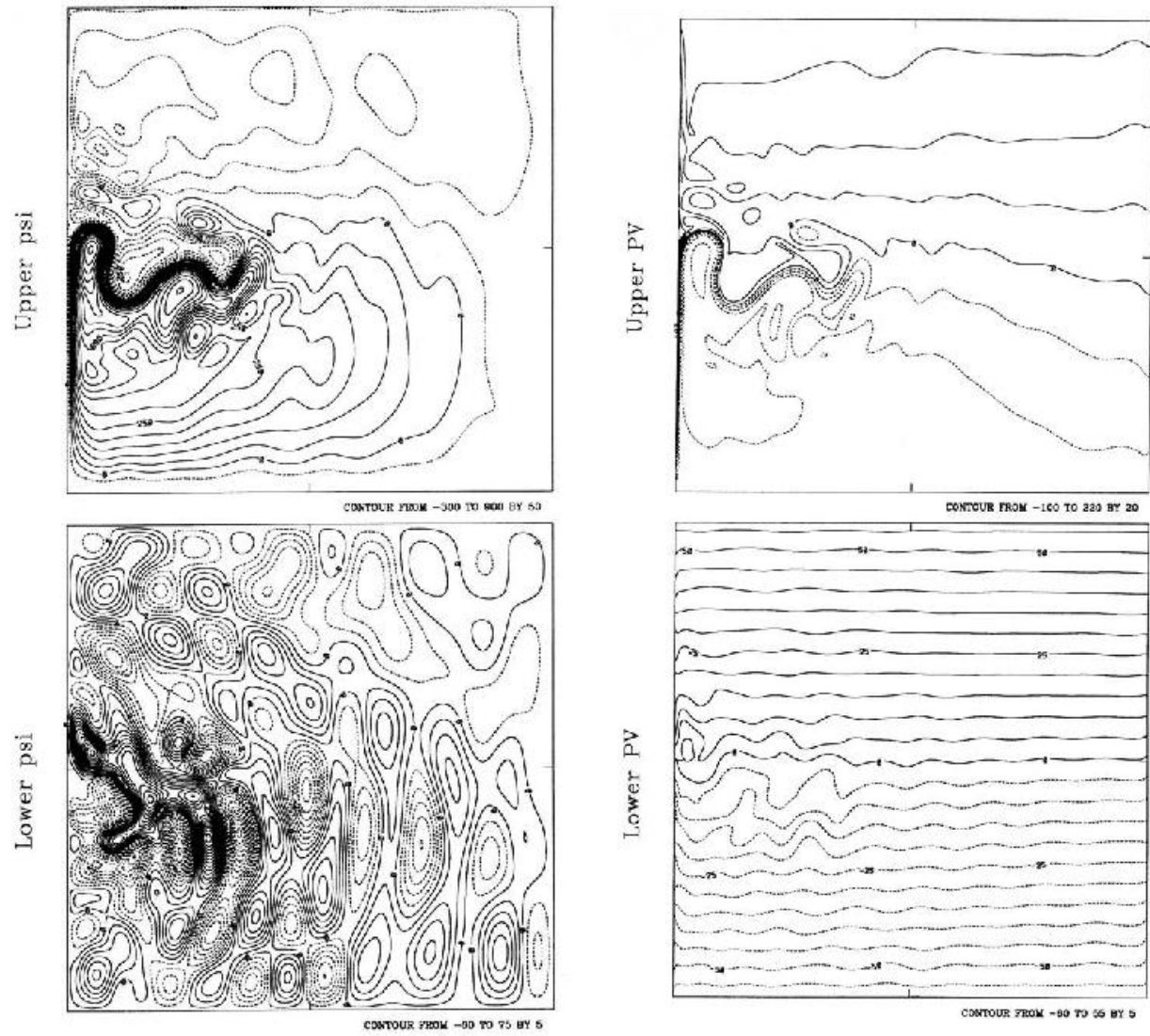
Figure 15: Solution 3: (c) instantaneous ψ_i & (d) instantaneous q_i.
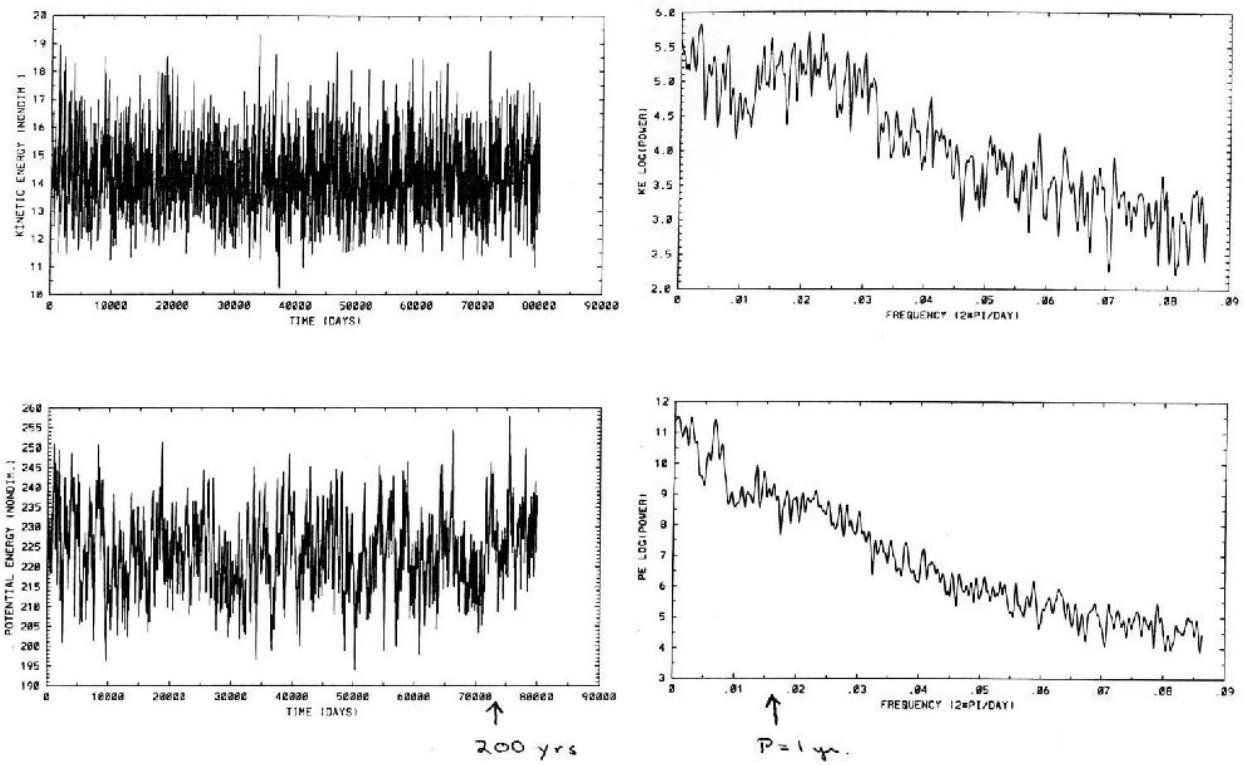
Figure 16: Solution 3: (e) energy time series & (f) energy spectra.
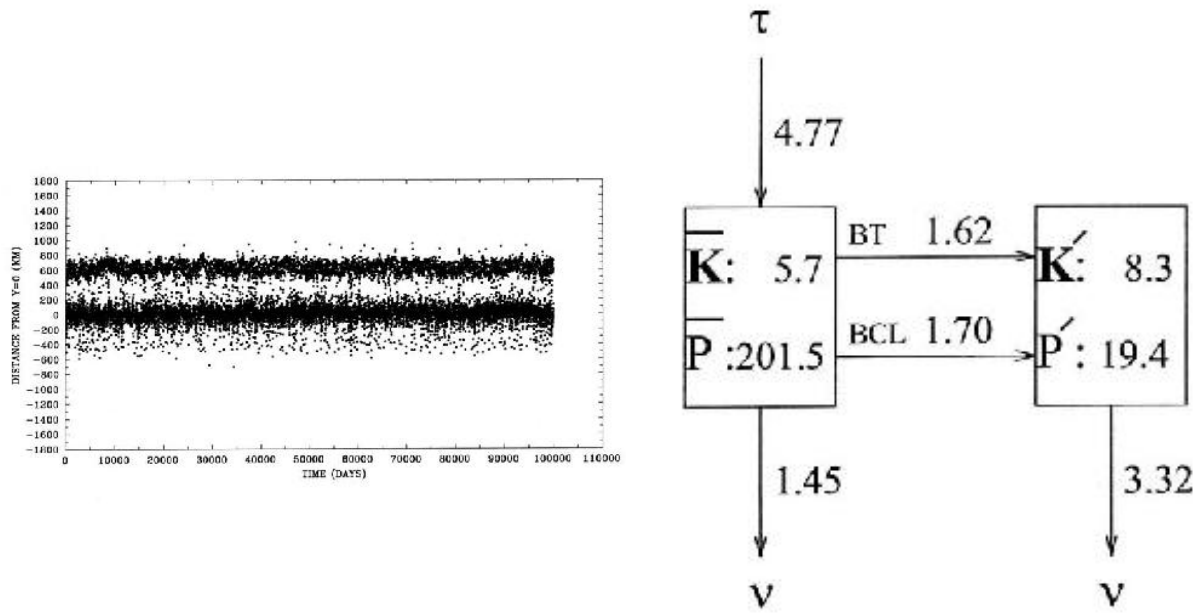
Figure 17: Solution 3: (g) WBC separation latitudes (analyzed at 5-day intervals) & (h) mean-eddy energy budget.
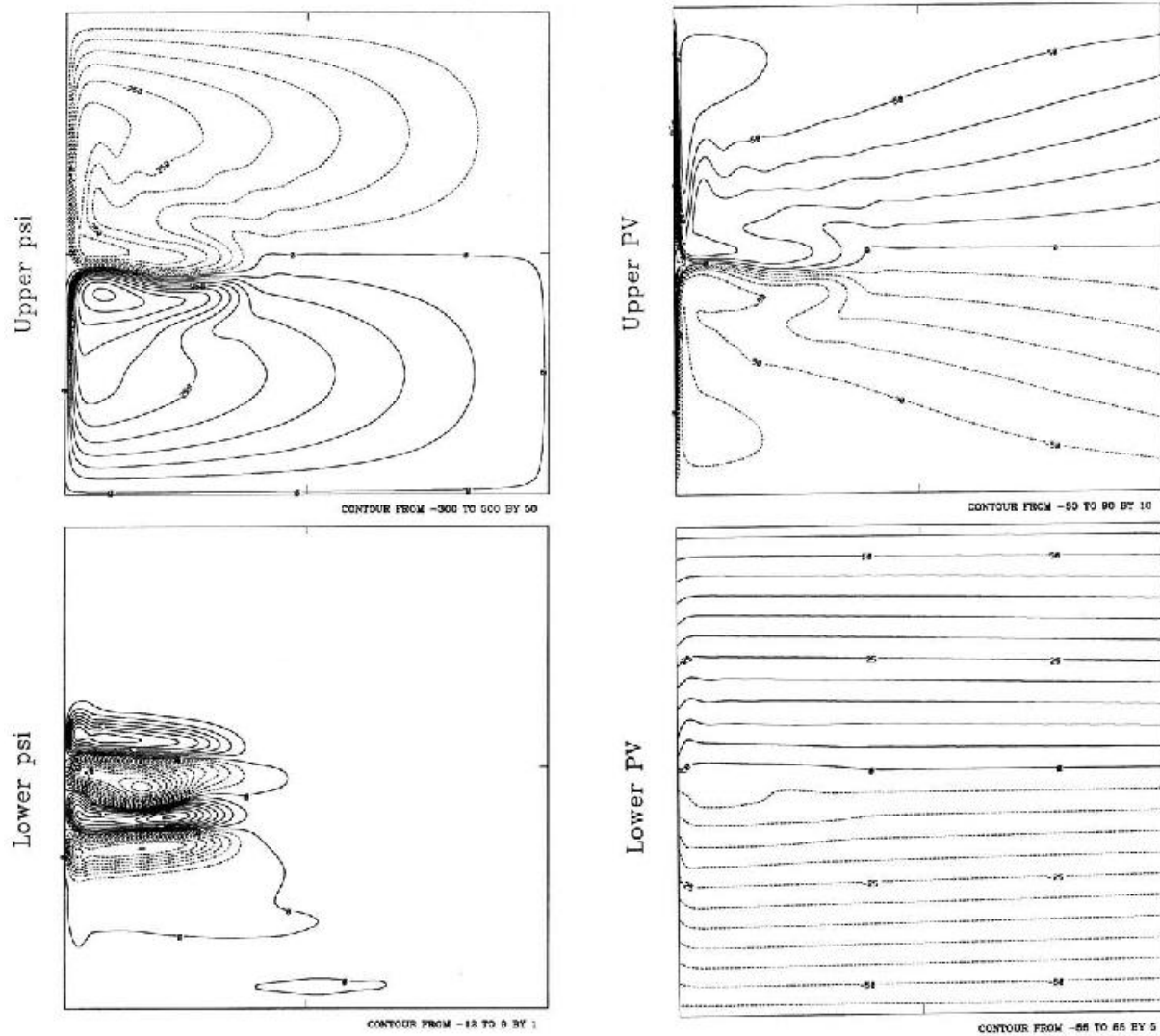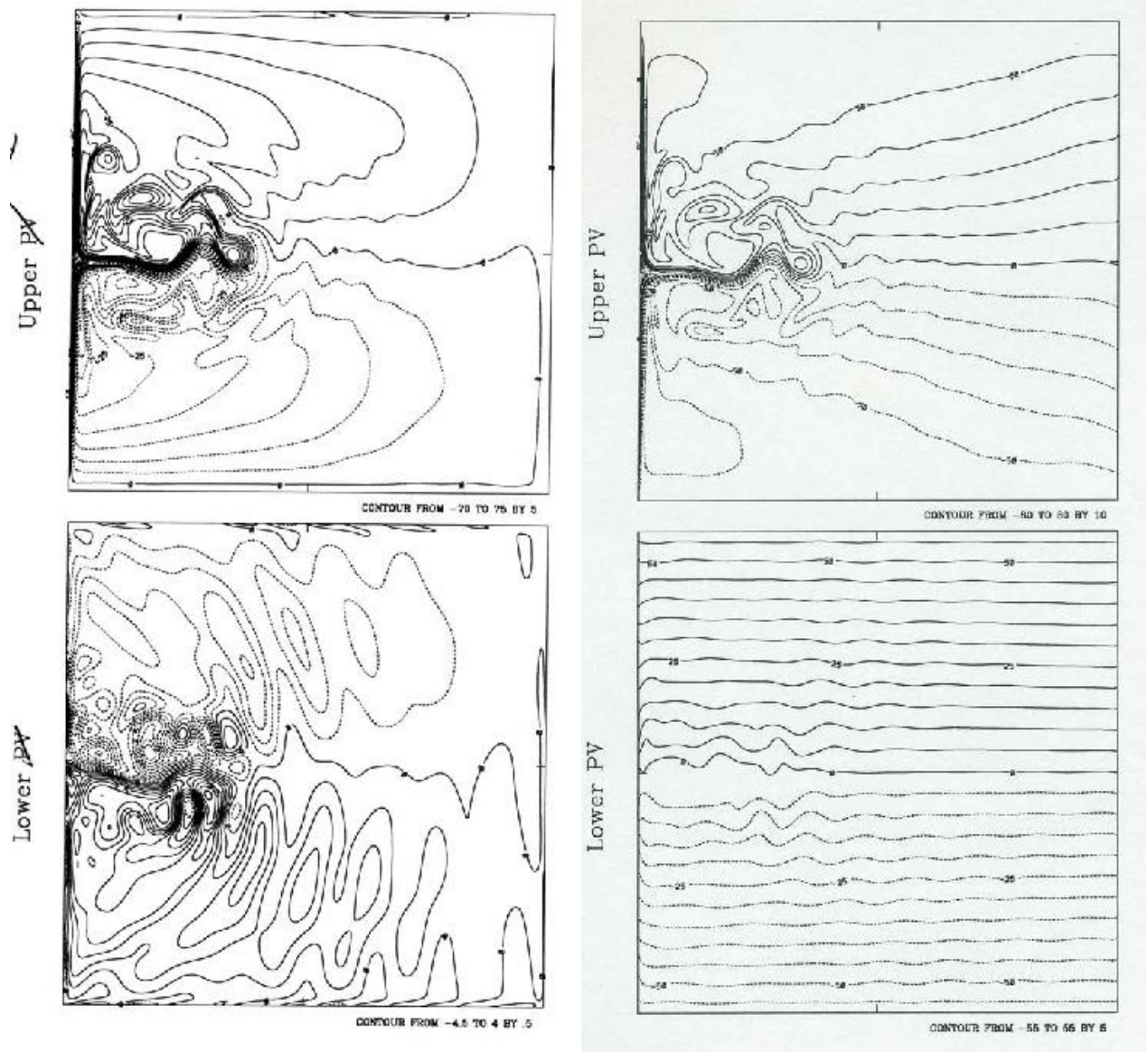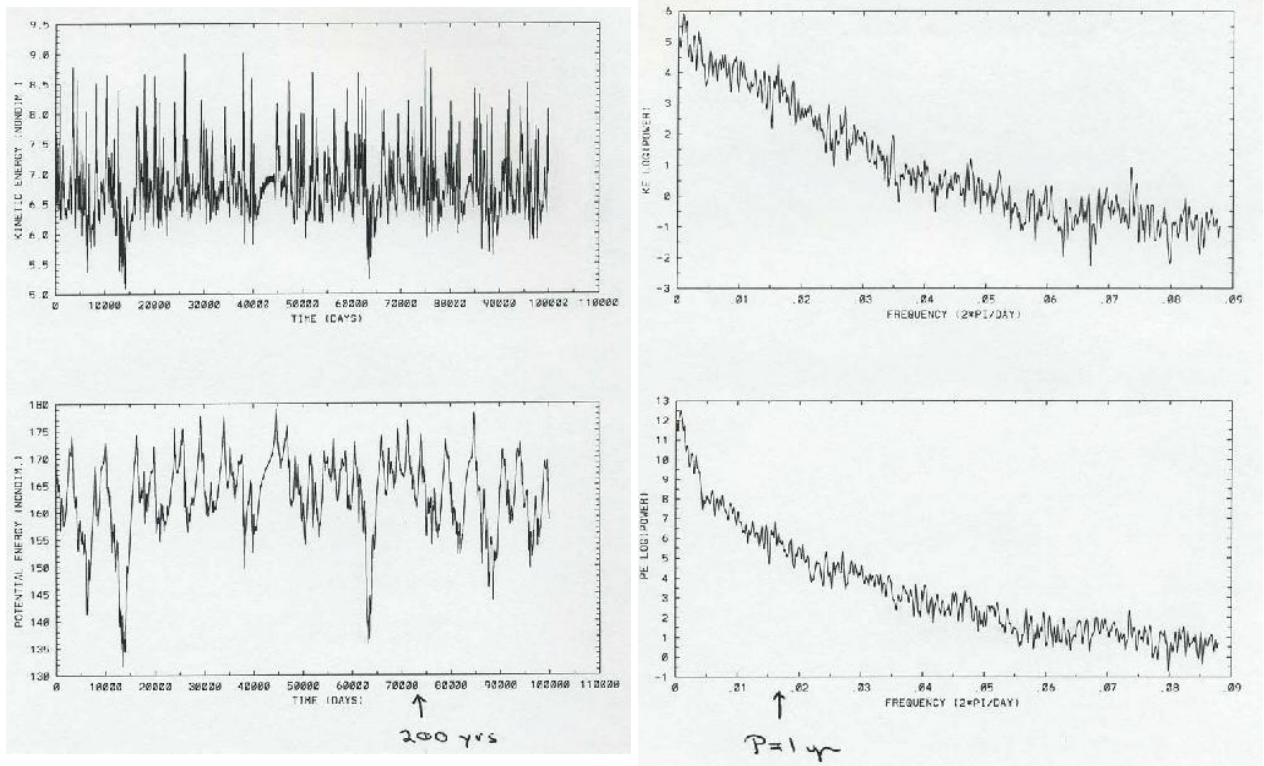
Upper psi

CONTOUR FROM −300 TO 300 BY 50

Upper PV

CONTOUR FROM −90 TO 90 BY 10

Lower psi

CONTOUR FROM −12 TO 0 BY 1

Lower PV

CONTOUR FROM −55 TO 55 BY 5

Figure 18: Solution 4: (a) $\overline{\psi}_i$ & (b) $\overline{q}_i$.

Figure 19: Solution 4: (c) instantaneous ψ_i & (d) instantaneous q_i.

Figure 20: Solution 4: (e) energy time series & (f) energy spectra.
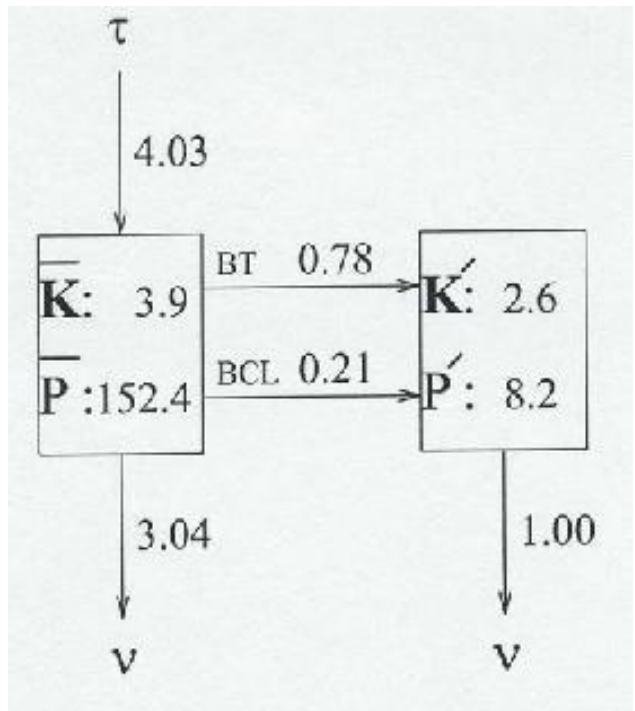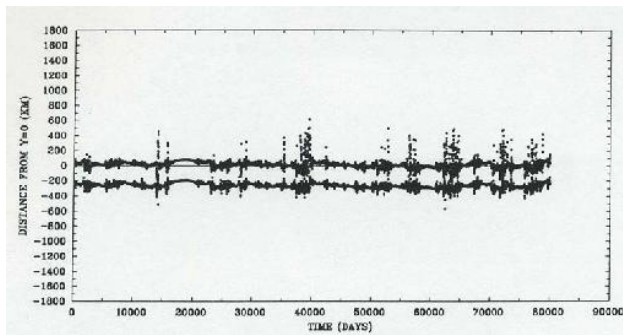
Figure 21: Solution 4: (g) WBC separation latitudes (analyzed at 5-day intervals) & (h) mean-eddy energy budget.
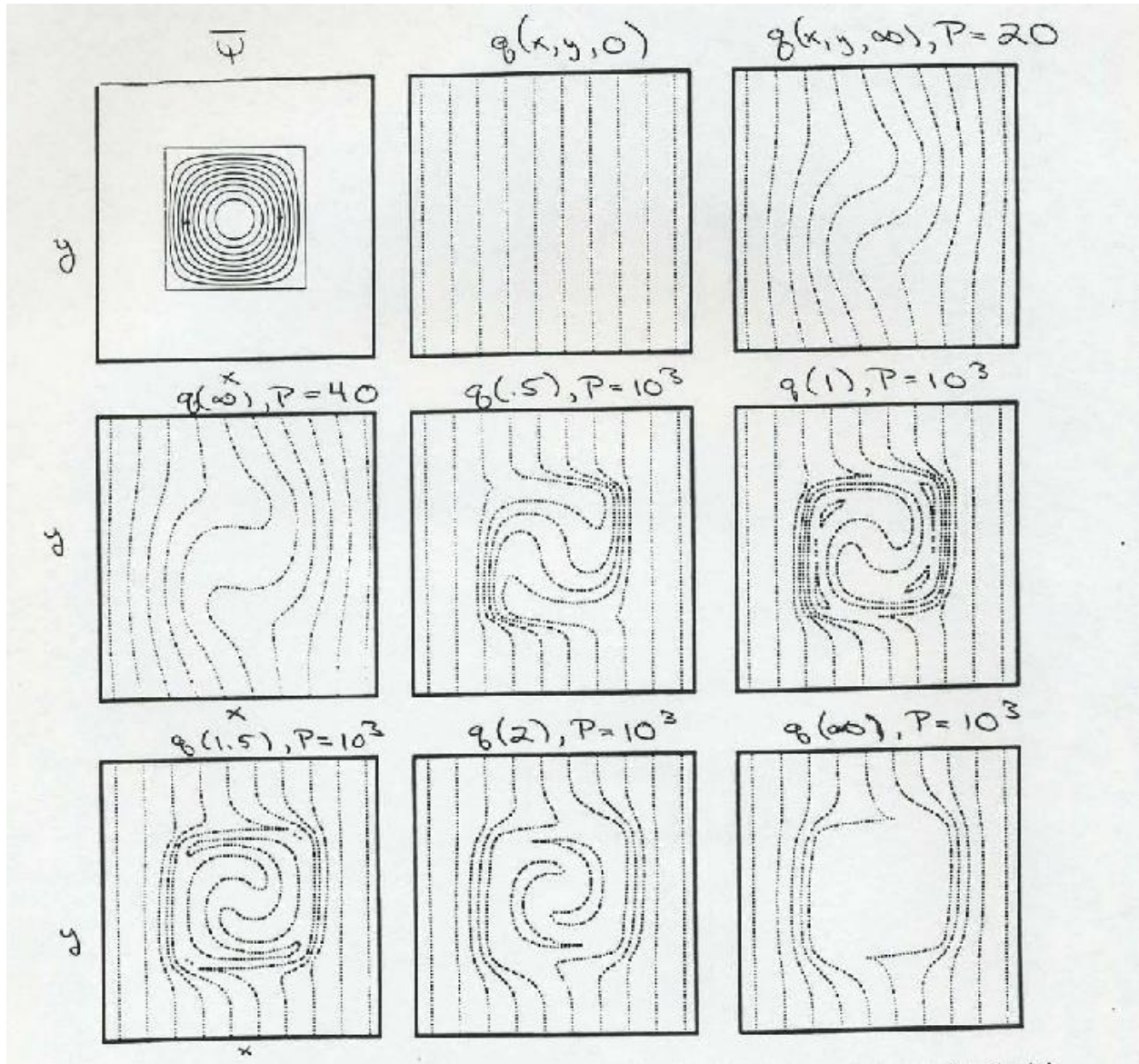
Figure 22: Homogenization of a passive tracer by a steady recirculation in a 2D flow Weiss (1966). $P = VL/\kappa$ is the Peclet number, and $q(x, y, t)$ is the passive tracer.
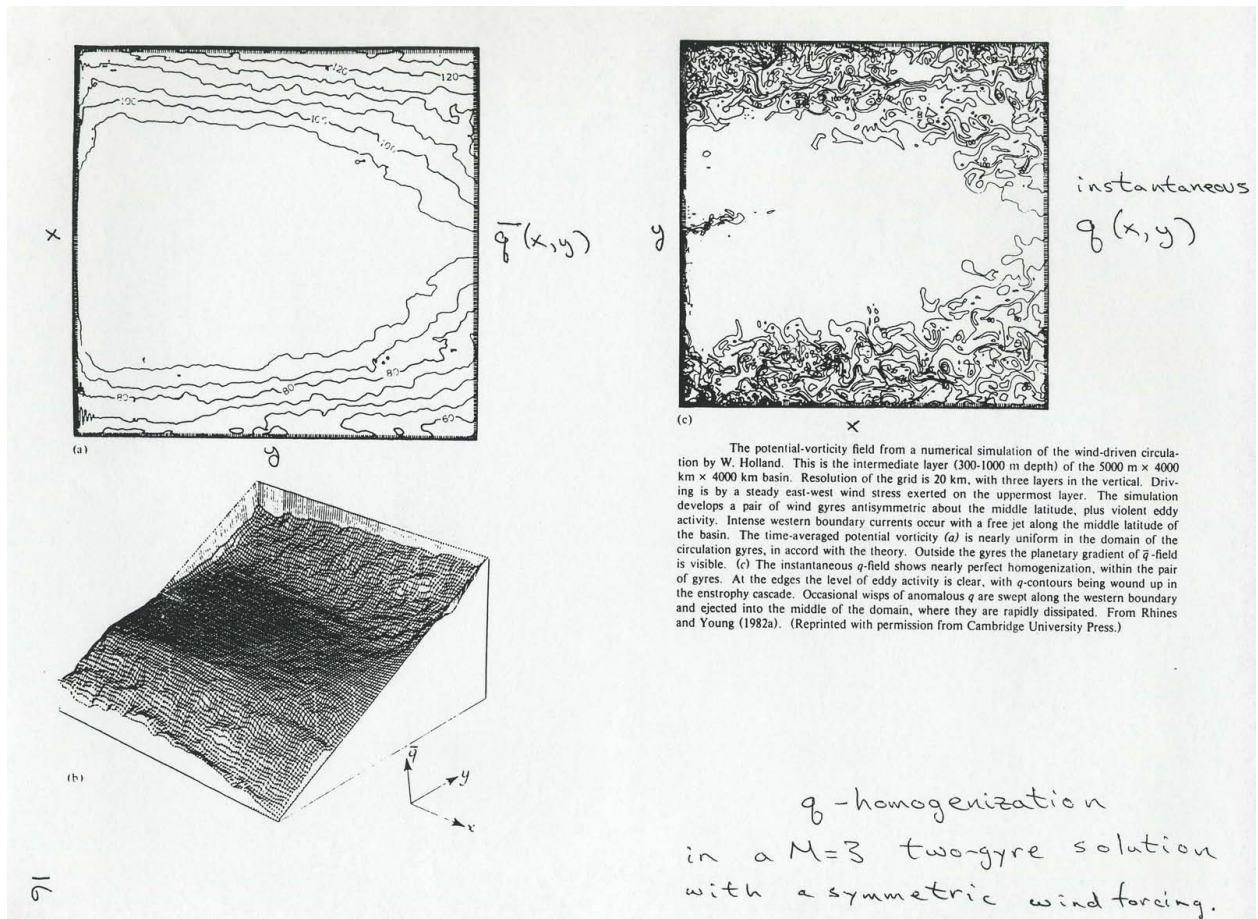
The potential-vorticity field from a numerical simulation of the wind-driven circulation by W. Holland. This is the intermediate layer (300-1000 m depth) of the 5000 m × 4000 km × 4000 km basin. Resolution of the grid is 20 km, with three layers in the vertical. Driving is by a steady east-west wind stress exerted on the uppermost layer. The simulation develops a pair of wind gyres antisymmetric about the middle latitude, plus violent eddy activity. Intense western boundary currents occur with a free jet along the middle latitude of the basin. The time-averaged potential vorticity *(a)* is nearly uniform in the domain of the circulation gyres, in accord with the theory. Outside the gyres the planetary gradient of $\bar{q}$-field is visible. *(c)* The instantaneous q-field shows nearly perfect homogenization, within the pair of gyres. At the edges the level of eddy activity is clear, with q-contours being wound up in the enstrophy cascade. Occasional wisps of anomalous q are swept along the western boundary and ejected into the middle of the domain, where they are rapidly dissipated. From Rhines and Young (1982a). (Reprinted with permission from Cambridge University Press.)

Figure 23: Homogenization of potential vorticity in the pycnocline at middle depths for a wind-gyre (Rhines and Young, 1982).

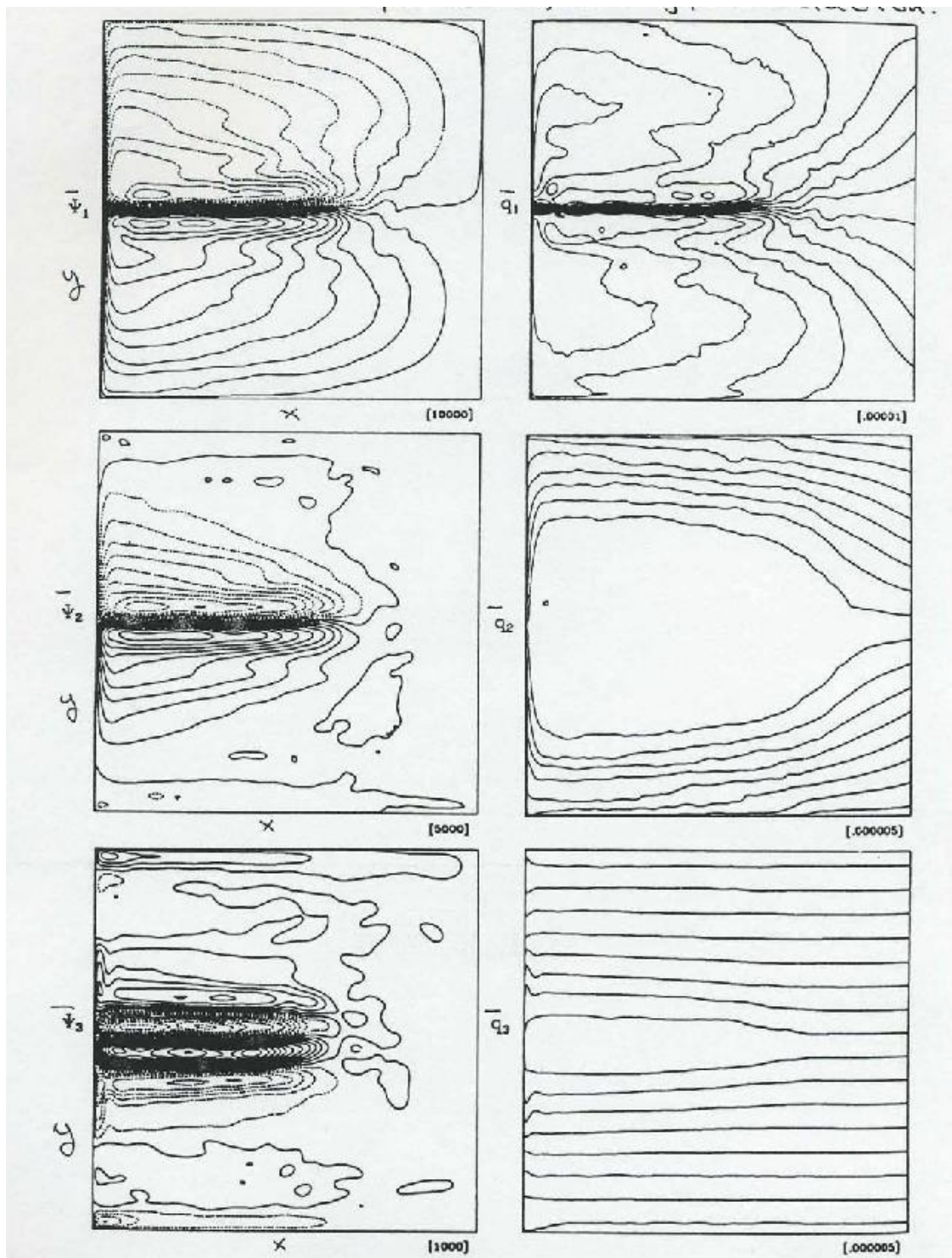Figure 24: $\overline{\psi}_i$ and $\overline{q}_i$ in a double-gyre, QG solution with $M = 3$ (Rhines and Schopf, 1991).

Maps of
$Q = fN^2$,
averaged in
time & over
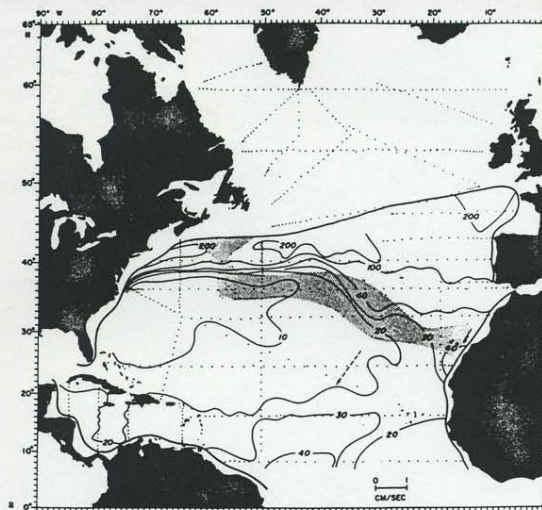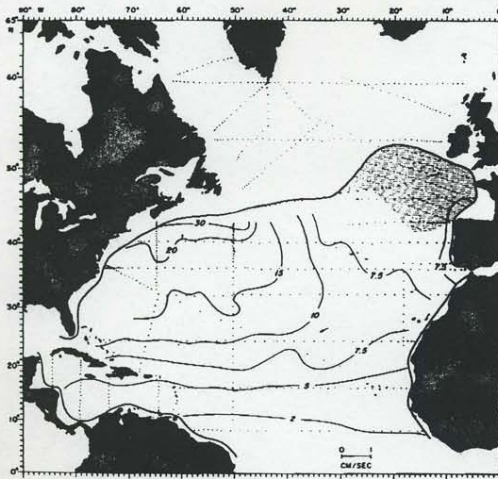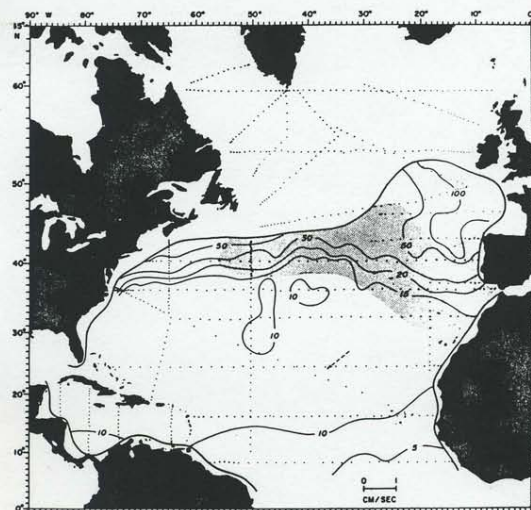a potential
density
interval

Fig. 3.11.3a–c. Planetary potential vorticity from hydrographic data for the North Atlantic at selected density intervals. a $\sigma_\theta = 26.3 - 26.5$. b $\sigma_\theta = 26.5 - 27$. Note the large region on nearly uniform potential vorticity. c $\sigma_\theta = 27.0 - 27.3$. (From McDowell et al. 1982)

(a) $\sigma_\theta = 26.3 - 26.5$

(b) $\sigma_\theta = 26.5 - 27.0$

(c) $\sigma_\theta = 27.0 - 27.3$

18

Figure 25: Observational analysis of planetary-geostrophic potential vorticity, $Q_{pg} = fN^2$ in the North Atlantic pycnocline (McDowell et al., 1982).

Figure 26: Interannual variation of wind-driven sea level from altimetry and barotropic streamfunction from a OGCM across the Kuroshio/Oyashio extension current in the North Pacific (Chelton and Mestas-Nunez, 1996). 1996).
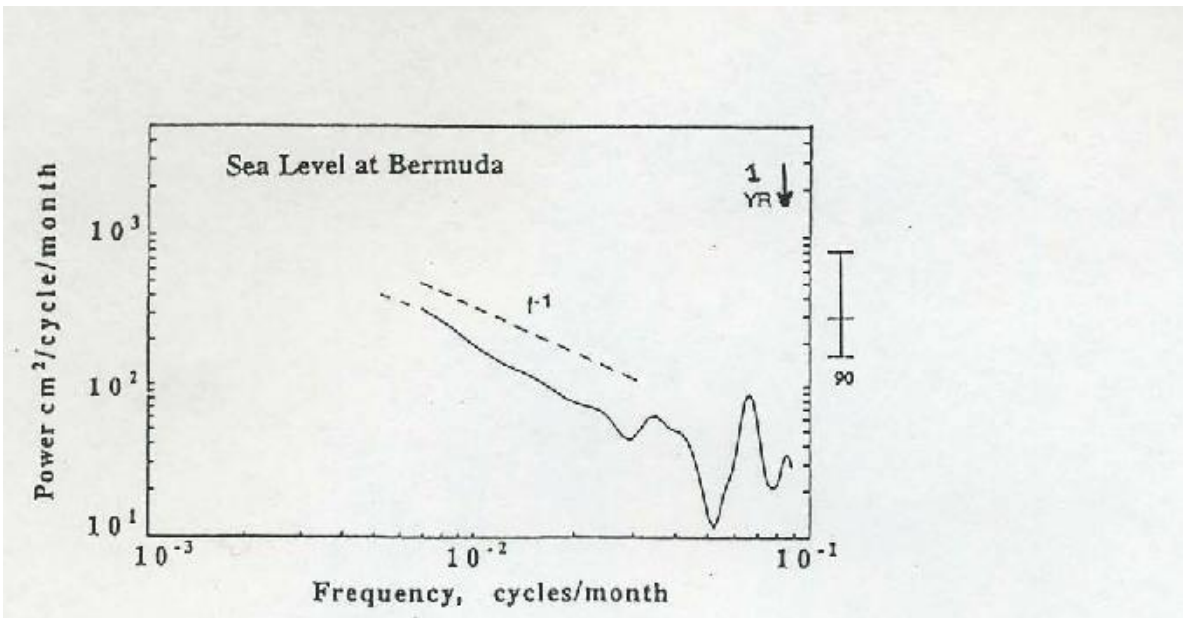
FIG. 2. Spectrum of sea level at Bermuda. Full curve shows a calculation from the continuous portion of data beginning in 1944, smoothed by three Hanning passes,
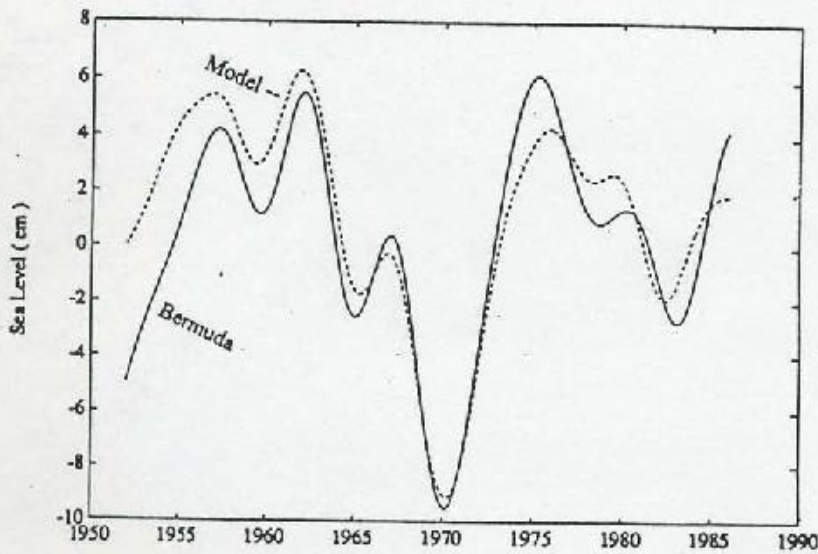

FIG. 4. Comparison between observed and computed sea level,

using

$$\frac{\partial \eta}{\partial t} - \beta R_i^2 \frac{\partial \eta}{\partial x} = -\frac{f^2 R_i^2}{g H_i} \; curl \left[\frac{\tau'}{f \rho_o} \right]$$

Figure 27: Decadal variation of wind-driven sea level at Bermuda, as measured and as calculated in (48) (Sturges and Hong, 1995).

References

Batchelor, G., 1956: On steady laminar flow with closed streamlines at large reynolds number. *J. Fluid Mech.*, **1**, 177–190.

Berloff, P. and J. McWilliams, 1999: Large-scale, low-frequency variability in wind-driven ocean gyres. *J. Phys. Ocean.*, **29**, 1925–1949.

Böning, C., 1986: On the influence of frictional parameterization in wind-driven ocean circulation models. *Dyn. Atm. Ocean*, **10**, 63–92.

Bryan, K., 1963: A numerical investigation of a nonlinear model of a wind-driven ocean. *J. Atmos. Sci.*, **20**, 594–606.

Charney, J., 1955: The gulf stream as an inertial boundary layer. *Proc. Natl. Acad. Sci. USA*, **41**, 731–740.

Chelton, D. and A. Mestas-Nunez, 1996: The large-scale, wind-driven response of the north pacific. *Int. WOCE Newsletter*, **No. 25**, 3–6.

Fofonoff, N., 1954: Steady flow in a frictionless homogeneous ocean. *J. Mar. Res.*, **13**, 254–262.

Gent, P. and J. McWilliams, 1990: Isopycnal mixing in ocean circulation models. *J. Phys. Ocean.*, **20**, 150–155.

Holland, W., 1986: Quasigeostrophic modeling of eddy-resolving ocean circulation. *Advanced Physcial Oceanographic Numerical Modeling*, J. O'Brien, ed., Reidel, 203–231.

Holland, W. and L. Lin, 1975: On the generation of mesoscale eddies and their contribution to the oceanic general circulation. I. A preliminary numerical experiment. *J. Phys. Ocean.*, **5**, 642–657.

Ireley, G. and V. Sheremet, 1995: Multiple solutions and inertial runaway of the wind driven circulation. *J. Mar. Res.*, **53**, 703–737.

Marshall, J., 1984: Eddy-mean flow interaction in a barotropic ocean model. *Quart. J. Roy. Meteor. Soc.*, **110**, 573–590.

McDowell, S., P. Rhines, and T. Keffer, 1982: North atlantic potential vorticity and its relation to the general circulation. *J. Phys. Ocean.*, **12**, 1417–1436.

Munk, W., 1950: On the wind-driven ocean circulation. *Journal of Meteorology*, **7**, 79–93.

Pedlosky, J., 1996: *Ocean Circulation Theory*. Springer-Verlag, 453 pp.

Rhines, P. and P. Schopf, 1991: The wind-driven circulation: Quasigeostrophic simulations and theory for nonsymmetric winds. *J. Phys. Ocean.*, **21**, 1438–1469.

Rhines, P. and W. Young, 1982: Homogenization of potential vorticity in planetary gyres. *J. Fluid Mech.*, **122**, 347–367.

Robinson, A., 1963: *Wind-driven Ocean Circulation: A Collection of Theoretical Studies*. Blaisdel, 161 pp.

Stommel, H., 1948: The westward intensification of wind-driven ocean currents. *Trans. Amer. Geophys. Union*, **29**, 202–206.

Sturges, W. and B. Hong, 1995: Wind forcing of the atlantic thermocline along 32 n at low frequencies. *J. Phys. Ocean.*, **25**, 1706–1715.

Sverdrup, H., 1947: Wind-driven currents in a baroclnic ocean: with application to the equatorial currents of the Eastern Pacific. *Proc. Natl. Acad. Sci. USA*, **33**, 318–326.

Veronis, G., 1966: Wind-driven ocean circulation. part ii. *Deep Sea Res.*, **13**, 30–55.

Weiss, N., 1966: The expulsion of magnetic flux by eddies. *Proc. Roy. Soc. London A*, **293**, 310–328.

Young, W., 1987: Baroclinic theories of the wind-driven circulation. *General Circulation of the Ocean*, H. Abarbanel and W. Young, eds., Springer-Verlag, 134–201.